

Origin of Aggregation-Induced Enhanced Emission: A Role of Pseudo-Degenerate Electronic States of Excimers Formed in Aggregation Phases

Wataru Ota,^{†,‡} Ken Takahashi,[¶] Kenji Higashiguchi,[§] Kenji Matsuda,[§] and Tohru Sato^{*,†,‡,||}

[†]*Fukui Institute for Fundamental Chemistry, Kyoto University, Sakyo-ku, Kyoto 606-8103, Japan*

[‡]*Department of Molecular Engineering, Graduate School of Engineering, Kyoto University, Nishikyo-ku, Kyoto 615-8510, Japan*

[¶]*Undergraduate School of Industrial Chemistry, Faculty of Engineering, Kyoto University, Nishikyo-ku, Kyoto 615 8510, Japan*

[§]*Department of Synthetic Chemistry and Biological Chemistry, Kyoto University, Nishikyo-ku, Kyoto 615-8510, Japan*

^{||}*Unit of Elements Strategy Initiative for Catalysts & Batteries, Kyoto University, Nishikyo-ku, Kyoto 615-8510, Japan*

E-mail: tsato@scl.kyoto-u.ac.jp

Abstract

Origin of aggregation-induced enhanced emission (AIEE) is investigated taking cyano-substituted 1,2-bis(pyridylphenyl)ethene (CNBE) as an example. On the basis of ONIOM calculations using the time-dependent density functional theory (TD-DFT), we found that pseudo-degeneracy of excimers formed in solid phase plays an important role in the appearance of the AIEE. The electron density difference delocalized over molecules gives the small diagonal vibronic coupling constants (VCCs), which suggests that the internal conversion is more suppressed in solid phase than in solution phase. The decrease of the off-diagonal VCCs by the packing effect is visualized by the vibronic coupling density (VCD) analysis. The pseudo-degeneracy enables the fluorescence from the high singlet excited states against the Kasha's rule because the electron density difference and the overlap density between excited states vanish. A Hubbard model of a pseudo-degenerate electronic system is constructed to elucidate the vanishing mechanism. We propose the following design principle for AIEE: *a candidate molecule for AIEE should have pseudo-degenerate adiabatic electronic states because of the excimer formation in aggregation states.*

Keywords

aggregation-induced enhanced emission, pseudo-degeneracy, vibronic coupling density, Kasha's rule

INTRODUCTION

In contrast to concentration quenching, aggregation-induced enhanced emission (AIEE) yields strong luminescence in aggregation phases.^{1,2} The restriction of intramolecular motions is generally accepted as a cause for the AIEE; that is, the restriction of intramolecular rotations or vibrations arising from physical constraint blocks non-radiative transition pathways.³ Hexaphenylsilole (HPS) is one of AIEE dyes, and the restricted rotation of side phenyl

ring is found to be a key factor for the AIEE.^{4–6} This is corroborated by quantum mechanical and molecular mechanical (QM/MM) calculations where the Huang–Rhys factors and reorganization energies at low-frequency modes are reduced in solid compared in gas phases by the packing effect.⁷ Also, HPS having bulky shape does not form a cofacial configuration in solid phase,^{1,2} which is considered to prevent concentration quenching.

A cofacial aggregation is regarded as one of the reasons for the concentration quenching. This is because a destructive alignment of the transition dipole moment makes the lowest excited state be symmetry forbidden.⁸ Nevertheless, some dyes have been reported to be emissive in spite of the formation of cofacial aggregations.^{9–16} In general, according to the Kasha's rule, emissions have been attributed to the lowest excited states.¹⁷ However, if all the radiative and non-radiative transitions from a high excited state to all the lower excited states than the high excited state are suppressed, the fluorescence from the high excited state can be expected to be possible against the Kasha's rule.

We have already reported that, in fluorescent dopants employed in organic light-emitting diode (OLED), radiative and non-radiative transitions from a triplet excited state T_n ($n > 1$) to all the lower triplet excited states can be suppressed due to the pseudo-degenerate electronic states.^{18–20} The pseudo-degeneracy gives the cancellation of the overlap density between excited states, which generates the T_n excitons with long lifetimes. This enables the fluorescence via higher triplets (FvHT) mechanism for OLEDs; that is the fluorescence utilizing the reverse intersystem crossing (RISC) from T_n to singlets. The FvHT is different from thermally activated delayed fluorescence (TADF) in that TADF undergoes the thermally activated RISC from T_1 to S_1 by decreasing their energy difference, $\Delta E_{S_1-T_1}$.^{21,22} The FvHT mechanism is proposed to explain the mechanism of the electroluminescence in some OLED dopants with large $\Delta E_{S_1-T_1}$ where T_1 excitons cannot thermally overcome the energy difference.^{19,23}

A cyano-substituted 1,2-bis(pyridylphenyl)ethene (CNBE) (Figure 1) has been reported to exhibit the AIEE behavior in solid phase.²⁴ The rate constant of the non-radiative transi-

tions are decreased from $> 1.0 \times 10^{10} \text{ s}^{-1}$ in CH_2Cl_2 solution to $5.0 \times 10^7 \text{ s}^{-1}$ in solid phase. Accordingly, the fluorescence quantum yield is increased from 0.002 to 0.72 by aggregation. Since CNBE forms cofacial configurations in solid phase, the occurrence of concentration quenching is predicted. Some cofacial CNBE molecules have C_i symmetry in the crystal structure. This suggests the possibility of pseudo-degenerate electronic states delocalized over the cofacial molecules. If this is the case, the fluorescence from higher singlets than S_1 is expected against the Kasha's rule because the transitions between the excited states can be suppressed as is the case in the FvHT mechanism. Furthermore, the electronic states delocalized over molecules may decrease vibronic coupling constants (VCCs).²⁵ This results indicate that the internal conversion can be more suppressed in solid than in solution phases as long as the excimer formation occurs in solid phase. In this study, we investigated the role of the pseudo-degeneracy on the appearance of the AIEE taking CNBE as an example. Vibronic coupling density (VCD) analyses were performed to elucidate the local picture of VCC.^{26–28} To explain the results obtained by the TD-DFT calculations, we discuss the electron density difference and overlap density in the pseudo-degenerate electronic system based on the Hubbard model.

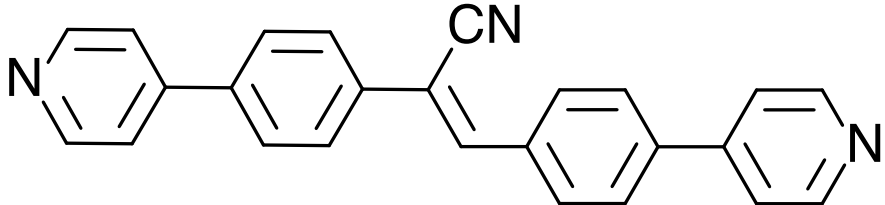


Figure 1: Chemical structure of cyano-substituted 1,2-bis(pyridylphenyl)ethene (CNBE).

THEORY

Consider the internal conversion from an initial vibronic state $|\Phi_{mi}(\mathbf{r}, \mathbf{Q})\rangle$ associated with electronic m and vibrational mi states to a final vibronic state $|\Phi_{nj}(\mathbf{r}, \mathbf{Q})\rangle$. Here, $\mathbf{r} = (\mathbf{r}_1, \dots, \mathbf{r}_i, \dots, \mathbf{r}_N)$ is a set of N electronic coordinates, and $\mathbf{Q} = (Q_1, \dots, Q_\alpha, \dots, Q_M)$ is a

set of M mass-weighted normal coordinates. Within the crude adiabatic approximation,^{29,30} the vibronic states are represented as the product of vibrational and electronic states fixed at nuclear configuration \mathbf{R}_0 : $|\Phi_{mi}(\mathbf{r}, \mathbf{Q})\rangle = |\chi_{mi}(\mathbf{Q})\rangle |\Psi_m(\mathbf{r}; \mathbf{R}_0)\rangle$. \mathbf{R}_0 is chosen as the equilibrium nuclear configurations at the ground or excited optimized structures. The rate constant of the internal conversion from electronic state m to n is expressed as³¹

$$k_{n \leftarrow m}^{\text{IC}}(T) = \frac{2\pi}{\hbar} \sum_{\alpha} |V_{mn,\alpha}|^2 \sum_{ij} P_{mi}(T) |\langle \chi_{mi} | Q_{\alpha} | \chi_{nj} \rangle|^2 \delta(E_{mi} - E_{nj}), \quad (1)$$

where $P_{mi}(T)$ is the Boltzmann distribution function of the initial vibronic state at temperature T , and E_{mi} and E_{nj} are the eigenenergies of $|\Phi_{mi}(\mathbf{r}, \mathbf{Q})\rangle$ and $|\Phi_{mi}(\mathbf{r}, \mathbf{Q})\rangle$, respectively. $V_{mn,\alpha}$ is the off-diagonal VCC given by

$$V_{mn,\alpha} = \left\langle \Psi_m(\mathbf{r}; \mathbf{R}_0) \left| \left(\frac{\partial \hat{H}(\mathbf{r}, \mathbf{R})}{\partial Q_{\alpha}} \right)_{\mathbf{R}_0} \right| \Psi_n(\mathbf{r}; \mathbf{R}_0) \right\rangle, \quad (2)$$

where $\hat{H}(\mathbf{r}, \mathbf{R})$ is the molecular Hamiltonian, and \mathbf{R} is a set of nuclear configuration. $V_n := V_{nn}$ is called the diagonal VCC. Ignoring the Duschinsky effect, which means vibrational modes do not change during an excitation, the matrix element of vibrational states is written as

$$\langle \chi_{mi} | Q_{\alpha} | \chi_{nj} \rangle = \langle n_{mi,\alpha} | Q_{\alpha} | n_{nj,\alpha} \rangle \prod_{\beta \neq \alpha} \langle n_{mi,\beta} | n_{nj,\beta} \rangle, \quad (3)$$

where $|n_{mi,\alpha}\rangle$ is a vibrational state of a single mode. The Franck–Condon (FC) overlap integral is expressed as³²

$$\langle n_{mi,\alpha} | n_{nj,\alpha} \rangle = \sqrt{\frac{n_{mi,\alpha}! n_{nj,\beta}!}{2^{n_{mi,\alpha} + n_{nj,\alpha}}}} e^{-\frac{1}{4}g_{n,\alpha}^2} \sum_{l=0}^{\min[n_{mi,\alpha}, n_{nj,\alpha}]} (-1)^{n_{mi,\alpha} - l} 2^l \frac{g_{n,\alpha}^{n_{mi,\alpha} + n_{nj,\alpha} - 2l}}{l!(n_{mi,\alpha} - 1)!(n_{nj,\alpha} - 1)!}. \quad (4)$$

Here, $g_{n,\alpha}$ is the dimensionless diagonal VCC (the Huang–Rhys factor):

$$g_{n,\alpha} = \frac{V_{n,\alpha}}{\sqrt{\hbar \omega_{n,\alpha}^3}}, \quad (5)$$

where $\omega_{n,\alpha}$ is the angular frequency of vibrational mode α . In general, a rate constant of an internal conversion is small when diagonal and off-diagonal VCCs are small.³¹ Particularly, the dependence of the rate constant on the diagonal VCC is strong, and the decrease of the diagonal VCCs significantly contributes to the suppression of the internal conversion.³¹

In addition to the internal conversion, vibrational relaxation from FC to adiabatic (AD) states is a non-radiative process that should be suppressed for emission.³¹ Within the crude adiabatic representation assuming the harmonic approximation, the reorganization energy due to vibrational relaxation is evaluated by

$$\Delta E = \sum_{\alpha} \frac{V_{n,\alpha}^2}{2\omega_{n,\alpha}^2}. \quad (6)$$

Thus, the decrease of the diagonal VCCs leads to the small reorganization energy that depends on the square of the diagonal VCCs.

The VCD is expressed as the density form of the VCC:^{26–28}

$$V_{mn,\alpha} = \int d\mathbf{x} \eta_{mn,\alpha}(\mathbf{x}), \quad (7)$$

where $\mathbf{x} = (x, y, z)$ is a three dimensional coordinate. The diagonal VCD $\eta_{n,\alpha}(\mathbf{x}) := \eta_{nn,\alpha}(\mathbf{x})$ is defined by

$$\eta_{n,\alpha}(\mathbf{x}) = \Delta\rho_{nm}(\mathbf{x}) \times v_{\alpha}(\mathbf{x}). \quad (8)$$

Here, $\Delta\rho_{nm}(\mathbf{x})$ is the electron density difference between $|\Psi_n(\mathbf{r}; \mathbf{R}_0)\rangle$ and the reference state $|\Psi_m(\mathbf{r}; \mathbf{R}_0)\rangle$:

$$\Delta\rho_{nm}(\mathbf{x}) = \langle \Psi_n(\mathbf{r}; \mathbf{R}_0) | \hat{\rho}(\mathbf{x}) | \Psi_n(\mathbf{r}; \mathbf{R}_0) \rangle - \langle \Psi_m(\mathbf{r}; \mathbf{R}_0) | \hat{\rho}(\mathbf{x}) | \Psi_m(\mathbf{r}; \mathbf{R}_0) \rangle. \quad (9)$$

$|\Psi_m(\mathbf{r}; \mathbf{R}_0)\rangle$ is taken as the electronic state in the equilibrium nuclear configuration. $\hat{\rho}(\mathbf{x})$ is

the electron density operator defined by

$$\hat{\rho}(\mathbf{x}) = \sum_{ij} \sum_{\sigma\tau} \hat{c}_{i\sigma}^\dagger \hat{c}_{j\tau} \psi_{i\sigma}^*(\mathbf{x}) \psi_{j\tau}(\mathbf{x}), \quad (10)$$

where $\psi_{i\sigma}^*(\mathbf{x})$ and $\psi_{j\tau}(\mathbf{x})$ are spatial orbitals, and $\hat{c}_{i\sigma}^\dagger$ and $\hat{c}_{j\tau}$ are creation and annihilation operators, respectively. i and j refer to the orbital indices, and σ and τ refer to the spin indices. $v_\alpha(\mathbf{x})$ is the potential derivative:

$$v_\alpha(\mathbf{x}) = \left(\frac{\partial u(\mathbf{x})}{\partial Q_\alpha} \right)_{\mathbf{R}_0}, \quad (11)$$

where $u(\mathbf{x})$ is the electron-nucleus potential acting on a single electron.

The off-diagonal VCD is defined by

$$\eta_{mn,\alpha}(\mathbf{x}) = \rho_{mn}(\mathbf{x}) \times v_\alpha(\mathbf{x}), \quad (12)$$

where $\rho_{mn}(\mathbf{x})$ is the overlap density between $|\Psi_m(\mathbf{r}; \mathbf{R}_0)\rangle$ and $|\Psi_n(\mathbf{r}; \mathbf{R}_0)\rangle$:

$$\rho_{mn}(\mathbf{x}) = \langle \Psi_m(\mathbf{r}; \mathbf{R}_0) | \hat{\rho}(\mathbf{x}) | \Psi_n(\mathbf{r}; \mathbf{R}_0) \rangle. \quad (13)$$

The VCD enables us to understand vibronic couplings (VCs) from the electronic factor $\Delta\rho_{nm}(\mathbf{x})$ or $\rho_{mn}(\mathbf{x})$ and the vibrational factor $v_\alpha(\mathbf{x})$. It should be noted that the disappearance of $\Delta\rho_{nm}(\mathbf{x})$ and $\rho_{mn}(\mathbf{x})$ give rise to the suppression of the internal conversions via the decrease of $V_{n,\alpha}$ and $V_{mn,\alpha}$, respectively. Since the transition dipole moment also depends on $\rho_{mn}(\mathbf{x})$,³¹ the disappearance of $\rho_{mn}(\mathbf{x})$ suppresses both the radiative and non-radiative transitions.

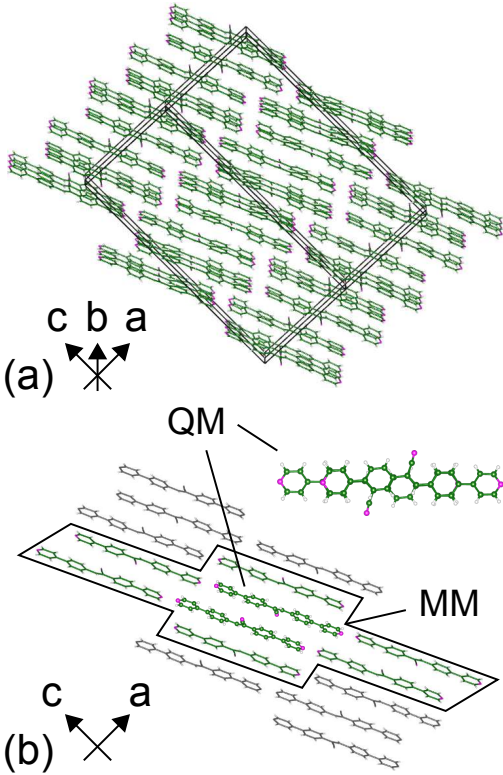


Figure 2: (a) Crystal structure of CNBE solid.²⁴ (b) Dimer Model **1** for the CNBE solid where centered cofacial molecules with C_i symmetry are selected as the QM region and the surrounding 16 molecules are selected as the MM region.

METHODS OF CALCULATIONS

Figure 2 (a) shows the crystal structure of the CNBE solid.²⁴ We modeled the CNBE solid as a dimer with a cofacial configuration (Figure 2 (b)), Dimer Model **1**, where the cofacial dimer were calculated by the QM method and surrounding 16 molecules were calculated by the MM method based on the ONIOM (our own *n*-layered integrated molecular orbital and molecular mechanics) approach.^{33,34} Dimer Model **1** belongs to C_i symmetry. The other dimer models aligned in different directions, Dimer Model **2** and Dimer Model **3** (see Figure S1 in the Supporting Information), belonging to C_1 symmetry were also investigated. The ground and excited states of the QM region were computed at the M06-2X/6-31G(d,p) and TD-M06-2X/6-31G(d,p) levels of theory, respectively, whereas the MM region was computed using the universal force field (UFF). The coordinates of the MM region were fixed during

the geometry optimizations and vibrational analyses for the ground and excited states.

The CNBE in CH_2Cl_2 solution was modeled as a single molecule with C_1 symmetry. The ground and excited states of a single molecule in solution, Monomer Model, were computed at the M06-2X/6-31G(d,p) and TD-M06-2X/6-31G(d,p) levels of theory, respectively, including the solvent effect through the polarizable continuum model (PCM).³⁵ The above calculations were carried out using the Gaussian 09.^{36,37} The VCCs and VCD were calculated using our own code.

RESULTS

There are a few possibilities for selecting dimers from the crystal structure. The total energies of excited states of the three kinds of dimer models were compared (Figure S2). The S_1 and S_2 states of Dimer Model **1** are energetically more stable than those of the other dimer models, and the fluorescence from Dimer Model **1** is expected. Therefore, we concentrate ourselves on Dimer Model **1**. Table 1 lists the excited states of Dimer Model **1** at the S_0 and S_2 optimized structures. From the selection rule of the electric dipole transition, S_1 (A_g) is symmetry-forbidden and S_2 (A_u) is symmetry-allowed (Laporté rule). Although, according to the Kasha's rule, an emission does not occur from the second excited states, the fluorescence from S_2 is possible if all the transitions from S_2 to S_1 are suppressed.

Table 1: Excited states of Dimer Model 1 at the S_0 and S_2 optimized structures. f denotes the oscillator strength.

State	Excitation energy			f	Major Configuration (CI coefficient)
	eV	nm			
@ S_0	S_1 (A_g)	3.7359	331.88	0.0000	HO-1 \rightarrow LU+1 (0.306), HO \rightarrow LU (0.622)
	S_2 (A_u)	3.9052	317.49	2.2807	HO-1 \rightarrow LU (0.366), HO \rightarrow LU+1 (0.585)
@ S_2	S_1 (A_g)	3.1397	394.89	0.0000	HO-1 \rightarrow LU+1 (0.212), HO \rightarrow LU (0.664)
	S_2 (A_u)	3.3074	374.86	1.8099	HO-1 \rightarrow LU (0.215), HO \rightarrow LU+1 (0.663)

Figures 3 (a) and (b) show the diagonal VCCs of S_0 @ S_2 and S_1 @ S_2 , respectively. Also, Figures 3 (c) and (d) show the off-diagonal VCCs of S_0 @ S_2 \leftarrow S_2 @ S_2 and S_1 @ S_2 \leftarrow S_2 @ S_2 ,

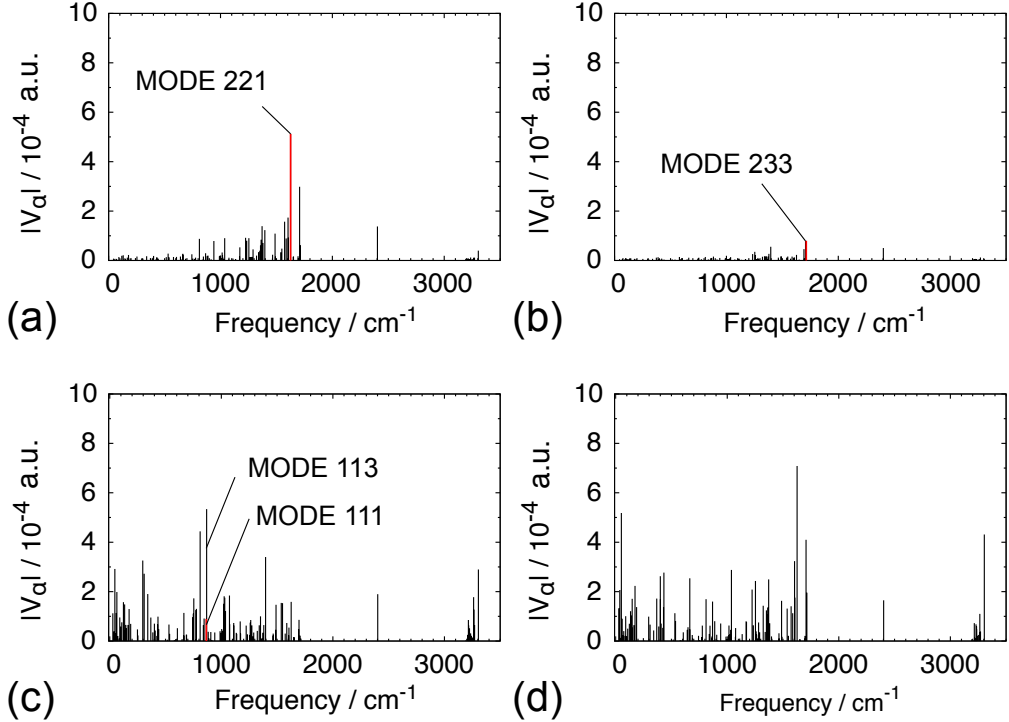


Figure 3: Diagonal VCCs of (a) $S_0 @ S_2$ and (b) $S_1 @ S_2$ as well as off-diagonal VCCs of (c) $S_0 @ S_2 \leftarrow S_2 @ S_2$ and (d) $S_1 @ S_2 \leftarrow S_2 @ S_2$ for Dimer Model 1.

respectively. The diagonal VCCs of $S_1 @ S_2$ are extremely small where the largest VCC of vibrational mode 233 is 0.79×10^{-4} a.u. In addition, both the off-diagonal VCCs of $S_1 @ S_2 \leftarrow S_2 @ S_2$ and $S_0 @ S_2 \leftarrow S_2 @ S_2$ are small. These results indicate that the internal conversions from S_2 to S_0 as well as to S_1 are suppressed while the radiative transition between S_2 and S_0 is allowed with the large oscillator strength (see Table 1). It should be noted, because of the extremely small diagonal VCCs of $S_1 @ S_2$, that the internal conversion from S_2 to S_1 is suppressed enabling the fluorescence from S_2 .

Figures 4 (a) and (b) show the frontier orbitals and orbital levels at the S_2 optimized structure, respectively. The adiabatic wave functions are delocalized over the molecules, thereby indicating the excimer formation in solid phase. In the present case, the delocalized electronic states are obtained because Dimer Model 1 belongs to C_i symmetry even in the AD state. The NHOMO and HOMO as well as the LUMO and NLUMO of the excimer are

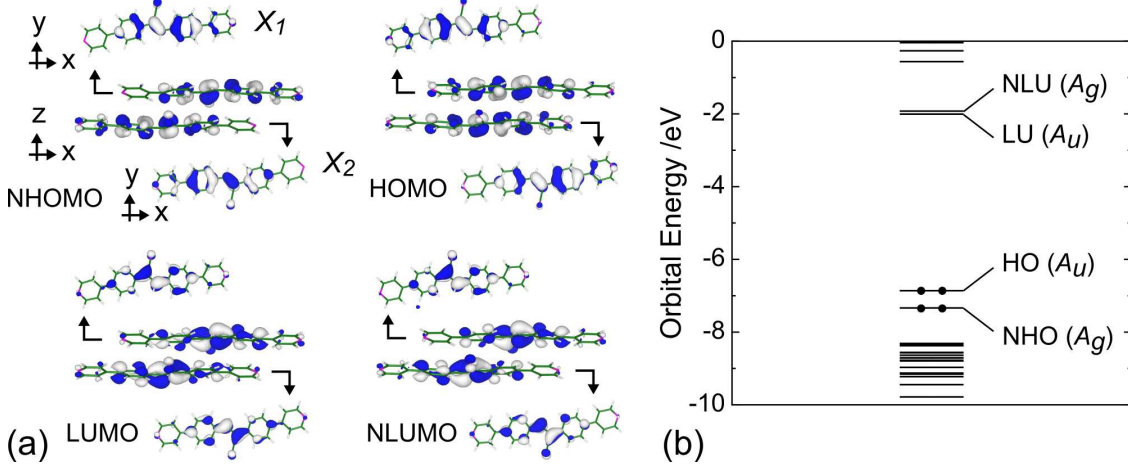


Figure 4: (a) Frontier orbitals and (b) orbital levels of Dimer Model **1** at the S_2 optimized structure. X_1 and X_2 are the constituent molecules of Dimer Model **1**. Isosurface values of the frontier orbitals are 3.0×10^{-2} a.u.

pseudo-degenerate, which are approximately expressed as

$$\psi_{\text{NHO}} \approx \frac{1}{\sqrt{2}}(\phi_{\text{HO}}(X_1) + \phi_{\text{HO}}(X_2)), \quad (14)$$

$$\psi_{\text{HO}} \approx \frac{1}{\sqrt{2}}(\phi_{\text{HO}}(X_1) - \phi_{\text{HO}}(X_2)), \quad (15)$$

$$\psi_{\text{LU}} \approx \frac{1}{\sqrt{2}}(\phi_{\text{LU}}(X_1) - \phi_{\text{LU}}(X_2)), \quad (16)$$

$$\psi_{\text{NLU}} \approx \frac{1}{\sqrt{2}}(\phi_{\text{LU}}(X_1) + \phi_{\text{LU}}(X_2)), \quad (17)$$

where $\phi_{\text{HO/LU}}(X_1/X_2)$ denotes the HOMO/LUMO of molecule X_1/X_2 consisted the model. $\phi_{\text{HO/LU}}(X_2)$ are obtained by a symmetry operation of $\phi_{\text{HO/LU}}(X_1)$. The frontier orbitals of the excimer are represented as the linear combinations of the HOMOs and LUMOs of the constituents with opposite signs.

S_1 mainly consists of the HOMO-LUMO and NHOMO-NLUMO excited configurations, whereas S_2 mainly consists of the HOMO-NLUMO and NHOMO-LUMO excited configurations (Table 1). Since the NHOMO/HOMO and LUMO/NLUMO are pseudo-degenerate, S_1 and S_2 are pseudo-degenerate. Figure 5 (a) and (b) show the electron density differences of $S_2@S_2-S_0@S_2$, $\Delta\rho_{20}$, and $S_1@S_2-S_0@S_2$, $\Delta\rho_{10}$, respectively. $\Delta\rho_{20}$ and $\Delta\rho_{10}$ exhibit simi-

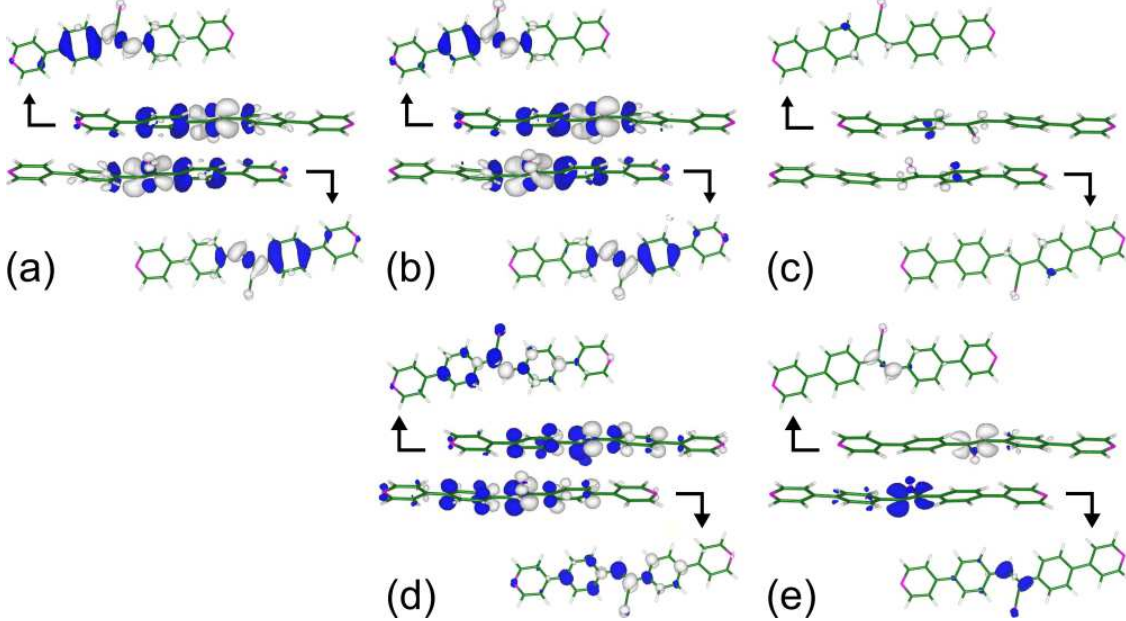


Figure 5: Electron density differences of (a) $S_1@S_2-S_0@S_2$, (b) $S_2@S_2-S_0@S_2$, and (c) $S_2@S_2-S_1@S_2$ of Dimer model 1. Isosurface values are 1.0×10^{-3} a.u. Overlap densities of (d) $S_2@S_2-S_0@S_2$, and (e) $S_2@S_2-S_1@S_2$ of Dimer model 1. Isosurface values are 2.0×10^{-3} a.u.

lar distributions. On the other hand, the electron density difference of $S_2@S_2-S_1@S_2$, $\Delta\rho_{21}$ (Figure 5 (c)) exhibits an extremely small distribution. This leads to the small diagonal VCD of $S_1@S_2$, resulting in the small diagonal VCCs of $S_1@S_2$. Figures 5 (d) and (e) show the overlap densities of $S_2@S_2-S_0@S_2$, ρ_{20} , and $S_2@S_2-S_1@S_2$, ρ_{21} , respectively. ρ_{21} exhibits a smaller distribution than that of ρ_{20} . The small ρ_{21} contributes to the small off-diagonal VCCs of $S_1@S_2 \leftarrow S_2@S_2$. From the distributions of the overlap densities, the off-diagonal VCCs of $S_0@S_2 \leftarrow S_2@S_2$ could be much larger than those of $S_1@S_2 \leftarrow S_2@S_2$. However, the values of these off-diagonal VCCs are comparable (Figures 3 (c) and (d)). This is because ρ_{20} is symmetrically localized on the atoms while ρ_{21} is localized on the bonds. In general, an overlap density symmetrically localized on atoms weakly couples to a potential derivative leading to small off-diagonal VCCs.³¹ Therefore, the off-diagonal VCCs of $S_0@S_2 \leftarrow S_2@S_2$ are not so large.

Consequently, the small electron density difference and overlap density between the pseudo-degenerate S_1 and S_2 excited states gives rise to the extremely small diagonal VCCs

of $S_1@S_2$ and the small off-diagonal VCCs of $S_1@S_2 \leftarrow S_2@S_2$. We will discuss the mechanism of the vanished electron density difference and overlap density in the pseudo-degenerate electronic system using the Hubbard model in Sec. 5.

In the following, we compare the VCs of Dimer Model **1** in solid with that of Monomer Model in solution. The reducible representation of vibrational modes for the monomer belonging to C_1 symmetry contains only A irreducible representations, and the number of the vibrational modes is

$$\Gamma_{\text{vib}}(C_1) = 129A, \quad (18)$$

where all the vibrational modes are vibronic active modes giving the non-zero diagonal and off-diagonal VCCs. On the other hand, the reducible representation for the dimer belonging to C_i symmetry is decomposed as

$$\Gamma_{\text{vib}}(C_i) = 132A_g + 132A_u, \quad (19)$$

where A_g and A_u are the totally and non-totally symmetric modes, respectively. The vibronic active mode for the diagonal VC is A_g and that for the off-diagonal VC is A_u . Therefore, the number of the vibronic active modes is almost the same in monomer and dimer although the total number of vibrational modes is increased in the dimer. The numbers of irreducible representations of vibrational modes in excimers with C_i , C_2 , and C_s symmetry are summarized in Section S2.

Figures 6 (a) and (b) show the diagonal VCCs of Monomer Model in the FC S_1 state and Dimer Model **1** in the FC S_2 state, respectively. The diagonal VCCs are greatly reduced by the excimer formation where the largest VCC of mode 109 in Monomer Model is 8.42×10^{-4} a.u. and that of mode 230 in Dimer Model **1** is 5.27×10^{-4} a.u. This result indicates that the internal conversion from S_2 to S_0 in Dimer Model **1** is suppressed in comparison with the one from S_1 to S_0 in Monomer Model because the rate constant of the internal conversion strongly depends on the diagonal VCCs.³¹ The off-diagonal VCCs of $S_0@S_1 \leftarrow S_1@S_1$ for Monomer

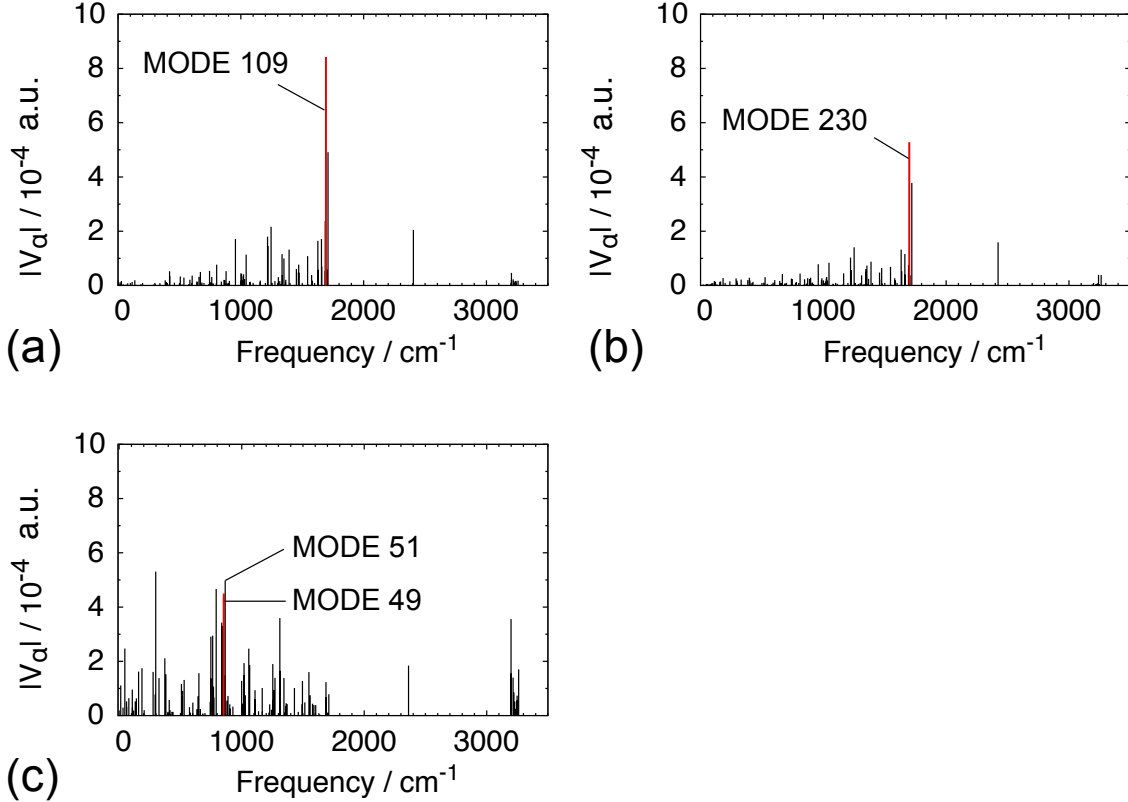


Figure 6: Diagonal VCCs (a) of Monomer Model in the FC S_1 state and (b) of Dimer Model **1** in the FC S_2 state. (c) Off-diagonal VCCs of $S_0@S_1 \leftarrow S_1@S_1$ of Monomer Model.

Model are presented in Figure 6 (c). The off-diagonal VCCs of Dimer Model **1** (Figure 3 (c)) are smaller than those of Monomer Model. For example, the off-diagonal VCC of mode 49 in Monomer Model is 4.49×10^{-4} and that of mode 111 in Dimer Model **1**, corresponding to mode 49 in Monomer Model, is 0.89×10^{-4} a.u. The decrease of the off-diagonal VCCs in Dimer Model **1** also contributes to the suppression of the internal conversion.

To shed light on the origin of the VCCs, the VCD analyses are performed. Figure 7 shows the results of the diagonal VCD analyses for the maximum coupling mode of Monomer Model and Dimer Model **1**. $\Delta\rho_{nm}(\mathbf{x})$ of Monomer Model strongly couples with $v_\alpha(\mathbf{x})$ of mode 109, leading to large $\eta_{n,\alpha}(\mathbf{x})$ particularly localized on the C=C bond. Thus, the spatial integration of $\eta_{n,\alpha}(\mathbf{x})$ of mode 109 gives the largest VCC. $\Delta\rho_{nm}(\mathbf{x})$, $v_\alpha(\mathbf{x})$, and $\eta_{n,\alpha}(\mathbf{x})$ of Dimer Model **1** are delocalized over the molecules. In general, delocalized $\Delta\rho_{nm}(\mathbf{x})$ and $v_\alpha(\mathbf{x})$ yield smaller diagonal VCCs than localized ones.²⁵ $\Delta\rho_{nm}(\mathbf{x})$ of X_1 (or X_2) exhibits a similar distribution

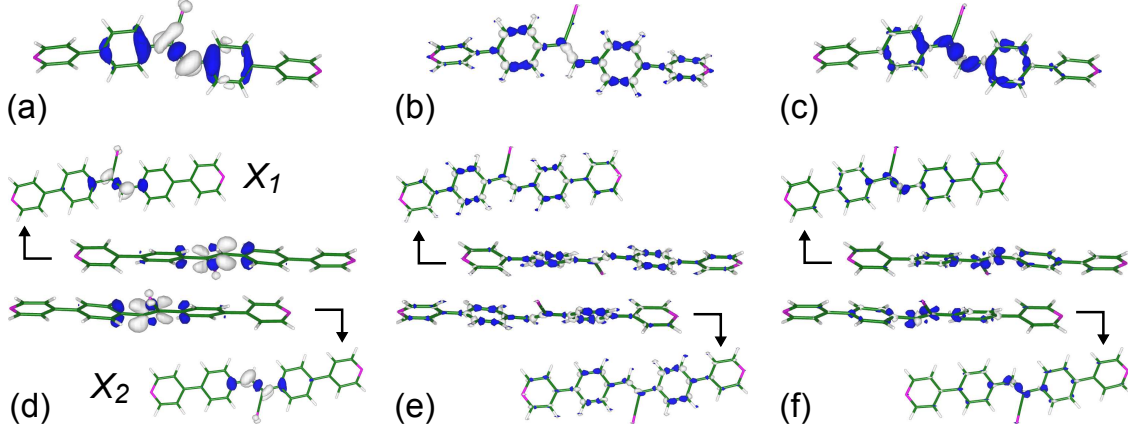


Figure 7: (a) Electron density difference, $\Delta\rho_{nm}(\mathbf{x})$, (b) potential derivative, $v_\alpha(\mathbf{x})$, and (c) diagonal VCD, $\eta_{n,\alpha}(\mathbf{x})$, of Monomer Model in the FC S_1 state for the maximum coupling mode (mode 109). (d) $\Delta\rho_{nm}(\mathbf{x})$, (e) $v_\alpha(\mathbf{x})$, and (f) $\eta_{n,\alpha}(\mathbf{x})$ of Dimer Model **1** in the FC S_2 state for the maximum coupling mode (mode 230). Isosurface values of $\Delta\rho_{nm}(\mathbf{x})$, $v_\alpha(\mathbf{x})$, and $\eta_{n,\alpha}(\mathbf{x})$ are 2.0×10^{-3} , 1.0×10^{-2} , and 1.0×10^{-5} a.u., respectively.

to that of Monomer Model. The value of $\Delta\rho_{nm}(\mathbf{x})$ of X_1 is one half of that of Monomer Model because the spatial integration of $\Delta\rho_{nm}(\mathbf{x})$ is zero by definition. In addition, $v_\alpha(\mathbf{x})$ of X_1 is $1/\sqrt{2}$ times that of Monomer Model owing to the normalized condition of vibrational modes. Since $\eta_{n,\alpha}(\mathbf{x})$ is expressed as the product of $\Delta\rho_{nm}(\mathbf{x})$ and $v_\alpha(\mathbf{x})$, the diagonal VCD of X_1 is $1/(2\sqrt{2})$ times that of Monomer Model. Therefore, the diagonal VCCs of Dimer Model **1**, obtained by the spatial integration of the diagonal VCD, are $1/\sqrt{2}$ times those of the Monomer Model. The ratio of the largest diagonal VCC of Dimer Model **1** to Monomer Model is 0.626, which is approximately equal to $1/\sqrt{2} \approx 0.707$ although the deviation occurs because the structures of X_1 and the monomer are not exactly the same.

In Dimer Model **1**, the decrease of the diagonal VCCs arises from the delocalized electronic states. In contrast, in Dimer Model **2** the electronic states are localized on a single molecule in the adiabatic excited states (Figure S3), which gives the properties of excited states similar to the monomer. Therefore, the decrease of the diagonal VCCs is not expected in Dimer Model **2**. The electronic states are delocalized over molecules in Dimer Model **3** (Figure S4), suggesting the small diagonal VCCs as in the case for Dimer Model **1**.

The driving force of the excimer formation is the diagonal VCCs. Figure 8 (a) shows the

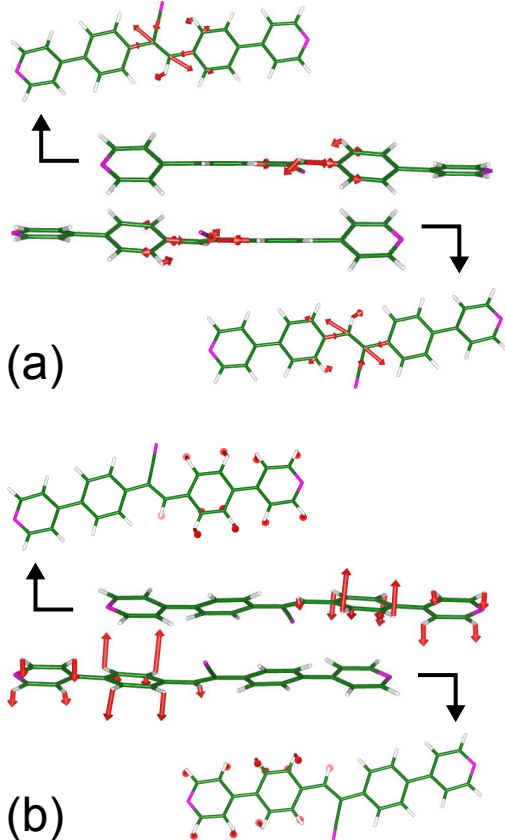


Figure 8: (a) Effective mode for the excimer formation of Dimer Model **1** in the FC S_2 state. This is an intramolecular vibration. (b) Vibrational mode 111 of Dimer Model **1** in the AD S_2 state of which the off-diagonal VCC is decreased by the packing effect. This is an intermolecular vibration.

effective mode for the excimer formation of Dimer Model **1** in the FC S_2 state. The effective mode is defined by the sum of normal modes weighted by the diagonal VCCs:

$$\xi = \sum_{\alpha} \frac{V_{n,\alpha}}{\sqrt{\sum_{\alpha} |V_{n,\alpha}|^2}} Q_{\alpha}, \quad (20)$$

which is the steepest descent direction of the vibrational relaxation.³⁸ The effective mode is the intramolecular vibration rather than the intermolecular one. This indicates that the excimer formation is induced by the intramolecular vibration.

Figure 9 shows the results of the off-diagonal VCD analyses of mode 49 for Monomer Model and mode 111 for Dimer Model **1**. $v_{49}(\mathbf{x})$ of Monomer Model is distributed over the stilbene unit. On the other hand, $v_{111}(\mathbf{x})$ of Dimer Model **1** is localized on one side of

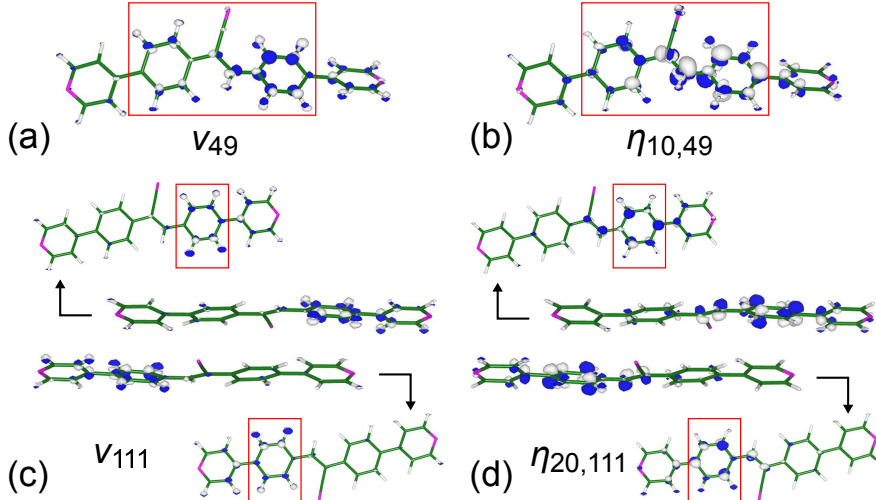


Figure 9: (a) Potential derivative, $v_\alpha(\mathbf{x})$, and (b) off-diagonal VCD, $\eta_{mn,\alpha}(\mathbf{x})$, of Monomer Model between $S_1 @ S_1$ and $S_0 @ S_1$. (c) $v_\alpha(\mathbf{x})$ and (b) $\eta_{mn,\alpha}(\mathbf{x})$ of Dimer Model **1** between $S_2 @ S_2$ and $S_0 @ S_2$. Isosurface values of $v_\alpha(\mathbf{x})$ and $\eta_{mn,\alpha}(\mathbf{x})$ are 1.0×10^{-2} and 1.0×10^{-5} a.u., respectively.

the stilbene unit. This is because the vibrational mode 111 is the intermolecular vibration (Figure 8 (b)) that is restricted by the surrounding molecules in solid phase. In other words, the localization of $v_\alpha(\mathbf{x})$ arises from the packing effect. As a result, $\eta_{mn,\alpha}(\mathbf{x})$ of Dimer Model **1** is also localized on one side of the stilbene unit giving the small off-diagonal VCCs. The degree of the localization of $v_\alpha(\mathbf{x})$ is expected to depend on the types of vibrational modes. The off-diagonal VCC of mode 51 in Monomer Model is 4.98×10^{-4} a.u. (Figure 6 (c)), which is comparable to that of mode 113 in Dimer Model **1**, 5.34×10^{-4} a.u., (Figure 3 (c)). Figure S5 shows $v_{51}(\mathbf{x})$ of Monomer Model and $v_{113}(\mathbf{x})$ of Dimer Model **1**. $v_{113}(\mathbf{x})$ of Dimer Model **1** is distributed over the stilbene unit rather than localized on one side of the stilbene unit in a similar manner to $v_{51}(\mathbf{x})$ of Monomer Model. This is because the vibrational mode 113 is the intramolecular vibration that is not easily affected by the surrounding molecules (Figure S5). Therefore, the off-diagonal VCCs corresponding to these modes are not reduced by the packing effect. The packing effect in solid phase is visualized by the potential derivative.

The small diagonal VCCs contributes to the suppression not only of the internal conversion but also of the vibrational relaxation.³¹ The reorganization energies due to vibrational relaxation were calculated to be $\Delta E = 0.582$ eV for Monomer Model and $\Delta E = 0.275$ eV for

Dimer Model **1**. For Monomer Model, since the potential energy surfaces of low-frequency torsional modes were not approximated to harmonic potentials, the reorganization energies for these vibrational modes were evaluated from the potential energy surfaces³¹ instead of using Eq. (6) (Figure S6). The reorganization energy of Dimer Model **1** is smaller than that of Monomer Model, and the suppressed vibrational relaxation is expected in Dimer Model **1**.

We also calculated the electronic states of Decamer Model for the CNBE solid (Figure S7). Decamer Model has the large oscillator strength in the FC S_8 state (Table S6), and the S_8 exciton expects to be generated by absorption. The electron density difference between the FC S_8 and S_0 states is delocalized as in the case for the combinations of Dimer Model **1** and **2** (Figure S8). The electronic states of Dimer Model **2** are localized on a single molecule after vibrational relaxation. Therefore, Decamer Model can be reduced to Dimer Model **1** in the adiabatic excited states. Thus, the modeling of the CNBE solid using Dimer Model **1** is considered to be reasonable.

DISCUSSION

In this section, we discuss the mechanism of the disappearances of the electron density difference and overlap density based on the Hubbard model. Consider an excited electronic structure of a system consisting of the same molecules X_1 and X_2 (Figure 10 (a)). Each molecule is not necessarily symmetric, but the dimer is assumed to have a symmetry such as C_i , C_2 , or C_s . For simplicity, only the HOMOs and LUMOs of X_1 and X_2 are considered. The energy gap between the HOMO and LUMO is expressed as ϵ . The hopping integrals for the HOMO-HOMO, LUMO-LUMO, and HOMO-LUMO between X_1 and X_2 are denoted by t_1 , t_2 , and t_3 , respectively. The Coulomb interactions for the HOMO-HOMO and HOMO-LUMO within X_1 or X_2 are denoted by U_1 and U_2 , respectively. Taking only a single excitation into account as done by the TD-DFT calculations, there are 9 electronic

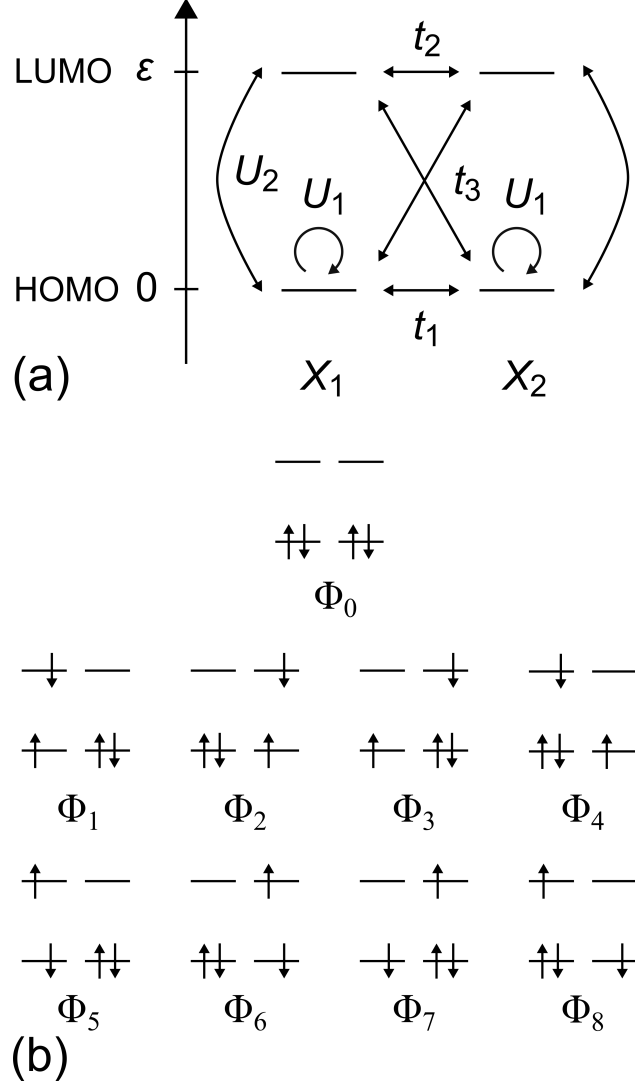


Figure 10: (a) Hubbard model of a system consisting of X_1 and X_2 . ϵ is the energy gap between the HOMO and LUMO. t_1 , t_2 , and t_3 are the hopping integrals for the HOMO-HOMO, LUMO-LUMO, and HOMO-LUMO, respectively, between X_1 and X_2 . U_1 and U_2 are the Coulomb interactions for the HOMO-HOMO and HOMO-LUMO, respectively, within X_1 or X_2 . (b) Electronic ground and excited configurations assuming a single excitation.

configurations (Figure 10 (b)) where $|\Phi_0\rangle$ is the ground configuration, $|\Phi_1\rangle$, $|\Phi_2\rangle$, $|\Phi_5\rangle$, and $|\Phi_6\rangle$ are locally-excited configurations, and $|\Phi_3\rangle$, $|\Phi_4\rangle$, $|\Phi_7\rangle$, and $|\Phi_8\rangle$ are charge-transfer configurations. t_1 , t_2 , and t_3 are considered to be small compared with U_1 and U_2 because t_1 , t_2 , and t_3 are the interactions between X_1 and X_2 separated from each other while U_1 and U_2 are the interactions within X_1 or X_2 . The model Hamiltonian for the basis defined

in Figure 10 (b) is given by

$$\begin{pmatrix} 2U_1 & 0 & 0 & t_3 & t_3 & 0 & 0 & t_3 & t_3 \\ \epsilon + U_1 + U_2 & 0 & t_2 & t_1 & 0 & 0 & 0 & 0 & 0 \\ \epsilon + U_1 + U_2 & t_1 & t_2 & 0 & 0 & 0 & 0 & 0 & 0 \\ \epsilon + U_1 + 2U_2 & 0 & 0 & 0 & 0 & 0 & 0 & 0 & 0 \\ \epsilon + U_1 + 2U_2 & 0 & 0 & 0 & 0 & 0 & 0 & 0 & 0 \\ \epsilon + U_1 + U_2 & 0 & t_2 & t_1 & t_2 & t_1 & 0 & 0 & 0 \\ \epsilon + U_1 + U_2 & t_1 & t_2 & 0 & 0 & 0 & 0 & 0 & 0 \\ \epsilon + U_1 + 2U_2 & 0 & 0 & 0 & 0 & 0 & 0 & 0 & 0 \end{pmatrix}. \quad (21)$$

Employing the Rayleigh–Schrödinger perturbation theory considering t_1 , t_2 , and t_3 as perturbations, the wavefunctions of the excited states are expressed as

$$|\Psi_1^s\rangle = \frac{1}{2}(|\Phi_1\rangle + |\Phi_5\rangle + |\Phi_2\rangle + |\Phi_6\rangle) - \frac{t_1 + t_2}{2U_2}(|\Phi_3\rangle + |\Phi_7\rangle + |\Phi_4\rangle + |\Phi_8\rangle), \quad (22)$$

$$|\Psi_2^s\rangle = \frac{1}{2}(|\Phi_3\rangle + |\Phi_7\rangle + |\Phi_4\rangle + |\Phi_8\rangle) + \frac{t_1 + t_2}{2U_2}(|\Phi_1\rangle + |\Phi_5\rangle + |\Phi_2\rangle + |\Phi_6\rangle), \quad (23)$$

$$|\Psi_1^a\rangle = \frac{1}{2}(|\Phi_1\rangle + |\Phi_5\rangle - |\Phi_2\rangle - |\Phi_6\rangle) - \frac{t_2 - t_1}{2U_2}(|\Phi_3\rangle + |\Phi_7\rangle - |\Phi_4\rangle - |\Phi_8\rangle), \quad (24)$$

$$|\Psi_2^a\rangle = \frac{1}{2}(|\Phi_3\rangle + |\Phi_7\rangle - |\Phi_4\rangle - |\Phi_8\rangle) + \frac{t_2 - t_1}{2U_2}(|\Phi_1\rangle + |\Phi_5\rangle - |\Phi_2\rangle - |\Phi_6\rangle), \quad (25)$$

where $|\Psi_1^s\rangle$ and $|\Psi_2^s\rangle$ are symmetric and $|\Psi_1^a\rangle$ and $|\Psi_2^a\rangle$ are antisymmetric wavefunctions. $|\Psi_1^s\rangle$ and $|\Psi_2^s\rangle$ belong to different symmetries from $|\Psi_1^a\rangle$ and $|\Psi_2^a\rangle$. The wavefunction of the ground state is expressed as

$$|\Psi_0\rangle = |\Phi_0\rangle - \frac{t_3}{\epsilon - U_1 + U_2}(|\Phi_3\rangle + |\Phi_7\rangle + |\Phi_4\rangle + |\Phi_8\rangle), \quad (26)$$

which depend on t_3 in contrast to the wavefunctions of the excited states.

Employing the Rayleigh–Schrödinger perturbation theory, the energies of the ground and

excited states are given by

$$E_0 = 2U_1 - \frac{4t_3^2}{\epsilon - U_1 + 2U_2}, \quad (27)$$

$$E_1^s = \epsilon + U_1 + U_2 - \frac{(t_1 + t_2)^2}{U_2}, \quad (28)$$

$$E_2^s = \epsilon + U_1 + 2U_2 + \frac{(t_1 + t_2)^2}{U_2}, \quad (29)$$

$$E_1^a = \epsilon + U_1 + U_2 - \frac{(t_2 - t_1)^2}{U_2}, \quad (30)$$

$$E_2^a = \epsilon + U_1 + 2U_2 + \frac{(t_2 - t_1)^2}{U_2}. \quad (31)$$

The energy difference between E_1^s and E_1^a as well as E_2^s and E_2^a is $|4t_1t_2/U_2|$. Since $4t_1t_2/U_2$ is assumed to be small, $|\Psi_1^s\rangle$ and $|\Psi_1^a\rangle$ as well as $|\Psi_2^s\rangle$ and $|\Psi_2^a\rangle$ are pseudo-degenerate. The orders of the excited states are $E_1^s \lesssim E_1^a < E_2^a \lesssim E_2^s$ for $t_1t_2 > 0$ and $E_1^a \lesssim E_1^s < E_2^s \lesssim E_2^a$ for $t_1t_2 < 0$: i.e. the symmetry of excited states changes according to the sign of the product t_1t_2 determined by the alignment of molecules. Degeneracies of the excited state occurs for $t_1t_2 = 0$. When t_1 , t_2 , and t_3 are no longer small compared to U_1 and U_2 , namely the perturbation theory is not valid, the degeneracy occurs in the case of $t_1 \neq 0$ or $t_2 \neq 0$ (see Figure S9).

When the system has C_i symmetry and $t_1t_2 > 0$, S_1 is symmetry-forbidden A_g and S_2 is symmetry-allowed A_u . This is the case for Dimer Model **1** of the CNBE solid. The electron density differences between S_1 ($|\Psi_1^s\rangle$) and S_0 ($|\Psi_0\rangle$) as well as S_2 ($|\Psi_1^a\rangle$) and S_0 are given by

$$\Delta\rho_{20} = \Delta\rho_{10} = \{(|\phi_{\text{LU}}(X_1)|^2 - |\phi_{\text{HO}}(X_1)|^2) - (|\phi_{\text{LU}}(X_2)|^2 - |\phi_{\text{HO}}(X_2)|^2)\}. \quad (32)$$

Thus, both $\Delta\rho_{20}$ and $\Delta\rho_{10}$ are expressed as the difference between the LUMOs and HOMOs of X_1 and X_2 . On the other hand, the electron density difference between S_2 and S_1 is expressed as

$$\Delta\rho_{21} = \Delta\rho_{20} - \Delta\rho_{10} = 0. \quad (33)$$

Therefore, $\Delta\rho_{21}$ is cancelled because $\Delta\rho_{20}$ and $\Delta\rho_{10}$ are the same due to the pseudo-degeneracy of S_1 and S_2 . The overlap density between S_2 and S_0 as well as S_2 and S_1 are given by

$$\rho_{20} = \frac{1}{\sqrt{2}} (\phi_{\text{HO}}(X_1)\phi_{\text{LU}}(X_1) - \phi_{\text{HO}}(X_2)\phi_{\text{LU}}(X_2)), \quad (34)$$

$$\rho_{21} = \frac{1}{2} \{ (|\phi_{\text{LU}}(X_1)|^2 - |\phi_{\text{HO}}(X_1)|^2) - (|\phi_{\text{LU}}(X_2)|^2 - |\phi_{\text{HO}}(X_2)|^2) \} \approx 0. \quad (35)$$

ρ_{20} is expressed as the non-vanishing product of HOMOs and LUMOs. In contrast, ρ_{21} is cancelled because this is expressed as the difference between the square of the HOMOs and LUMOs. The other pairs of the electron density differences and overlap densities in the pseudo-degenerate electronic system are summarized in Table S7 and Table S8, respectively.

CONCLUDING REMARKS

The origin of the AIEE in the CNBE solid is investigated by the ONIOM method using the TD-DFT calculations. The pseudo-degeneracy arising from the excimer formation in solid phase gives the cancellation of the electron density difference and overlap density between S_1 and S_2 , which suggests that the fluorescence from the second excited state is possible against the Kasha's rule because the transitions from the second to first excited states are suppressed. The electronic states delocalized over the molecules reduce the diagonal VCCs in solid phase to approximately $1/\sqrt{2}$ times those in solution phase. In addition, the packing effect in solid phase reduce the off-diagonal VCCs of the intermolecular vibrations. These results indicate that the internal conversion from excited to ground states is more suppressed in solid phase than in solution phase.

In the present study, we discussed a dimer with the C_i site symmetry. Another cyano-substituted compounds exhibiting AIEE such as bis(4-bromophenyl)-fumaronitrile, bis(3-trifluoromethylphenyl)fumaronitrile, bis(4-methoxyphenyl)-fumaronitrile,³⁹ and oligo(*para*-

phenylene vinylene) (CN-DPDSB)⁴⁰ also have C_i site symmetry in their crystal structures, which suggests that AIEE occurs due to the pseudo-degeneracy in these compounds. It should be noted, however, that the other symmetries including C_1 could be also possible for the appearance of the AIEE as long as the pseudo-degenerate electronic states are generated in aggregation phase.

A molecule which forms excimers with delocalized excited electronic wavefunction can be fluorescent in aggregation phase, even if the molecule is not fluorescent in an isolated state such as solution or vacuum. Accordingly, we can obtain the following design principle for AIEE: *a candidate molecule for AIEE should have pseudo-degenerate adiabatic electronic states because of the excimer formation in aggregation states.*

Acknowledgement

This study was supported by JSPS KAKENHI Grant Number JP17H05259 in Scientific Research on Innovative Areas "Photosynergetics". Numerical calculations were partly performed at Supercomputer System, Institute for Chemical Research, Kyoto University, Academic Center for Computing and Media Studies (ACCMS), Kyoto University, and Research Center for Computational Science, Okazaki.

Supporting Information Available

The following files are available free of charge.

References

- (1) Hong, Y.; Lam, J. W. Y.; Tang, B. Z. Aggregation-Induced Emission: Phenomenon, Mechanism and Applications. Chem. Commun. **2009**, 4332–4353.

(2) Hong, Y.; Lam, J. W. Y.; Tang, B. Z. Aggregation-Induced Emission. *Chem. Soc. Rev.* **2011**, 40, 5361–5388.

(3) Mei, J.; Hong, Y.; Lam, J. W. Y.; Qin, A.; Tang, Y.; Tang, B. Z. Aggregation-Induced Emission: the Whole is More Brilliant than the Parts. *Adv. Mater.* **2014**, 26, 5429–5479.

(4) Chen, J.; Law, C. C. W.; Lam, J. W. Y.; Dong, Y.; Lo, S. M. F.; Williams, I. D.; Zhu, D.; Tang, B. Z. Synthesis, Light emission, Nanoaggregation, and Restricted Intramolecular Rotation of 1,1-Substituted 2,3,4,5-Tetraphenylsiloles. *Chem. Mater.* **2003**, 15, 1535–1546.

(5) Yu, G.; Yin, S.; Liu, Y.; Chen, J.; Xu, X.; Sun, X.; Ma, D.; Zhan, X.; Peng, Q.; Shuai, Z.; Tang, B.; Zhu, D.; Fang, W.; Luo, Y. Structures, Electronic states, Photoluminescence, and Carrier Transport Properties of 1,1-Disubstituted 2,3,4,5-Tetraphenylsiloles. *J. Am. Chem. Soc.* **2005**, 127, 6335–6346.

(6) Zhao, Z.; He, B.; Tang, B. Z. Aggregation-Induced Emission of Siloles. *Chem. Sci.* **2015**, 6, 5347–5365.

(7) Zhang, T.; Jiang, Y.; Niu, Y.; Wang, D.; Peng, Q.; Shuai, Z. Aggregation Effects on the Optical Emission of 1,1,2,3,4,5-Hexaphenylsilole (HPS): a QM/MM Study. *J. Phys. Chem. A* **2014**, 118, 9094–9104.

(8) Cornil, J.; Beljonne, D.; Calbert, J.-P.; Brédas, J.-L. Interchain Interactions in Organic π -Conjugated Materials: Impact on Electronic Structure, Optical Response, and Charge Transport. *Adv. Mater.* **2001**, 13, 1053–1067.

(9) Rösch, U.; Yao, S.; Wortmann, R.; Würthner, F. Fluorescent H-aggregates of Merocyanine Dyes. *Angew. Chem.* **2006**, 118, 7184–7188.

(10) Yoon, S.-J.; Chung, J. W.; Gierschner, J.; Kim, K. S.; Choi, M.-G.; Kim, D.; Park, S. Y. Multistimuli Two-Color Luminescence Switching via Different Slip-Stacking of Highly Fluorescent Molecular Sheets. *J. Am. Chem. Soc.* **2010**, 132, 13675–13683.

(11) Yao, H.; Ashiba, K. Highly Fluorescent Organic Nanoparticles of Thiacyanine Dye: A Synergetic Effect of Intermolecular H-aggregation and Restricted Intramolecular Rotation. *RSC Adv.* **2011**, 1, 834–838.

(12) Wang, L.; Shen, Y.; Yang, M.; Zhang, X.; Xu, W.; Zhu, Q.; Wu, J.; Tian, Y.; Zhou, H. Novel Highly Emissive H-aggregates with Aggregate Fluorescence Change in a Phenylbenzoxazole-Based System. *Chem. Commun.* **2014**, 50, 8723–8726.

(13) Basak, S.; Nandi, N.; Bhattacharyya, K.; Datta, A.; Banerjee, A. Fluorescence from an H-aggregated Naphthalenediimide Based Peptide: Photophysical and Computational Investigation of This Rare Phenomenon. *Phys. Chem. Chem. Phys.* **2015**, 17, 30398–30403.

(14) Lucenti, E.; Forni, A.; Botta, C.; Carlucci, L.; Giannini, C.; Marinotto, D.; Previtali, A.; Righetto, S.; Cariati, E. H-Aggregates Granting Crystallization-Induced Emissive Behavior and Ultralong Phosphorescence from a Pure Organic Molecule. *J. Phys. Chem. Lett.* **2017**, 8, 1894–1898.

(15) Qian, H.; Cousins, M. E.; Horak, E. H.; Wakefield, A.; Liptak, M. D.; Aprahamian, I. Suppression of Kasha’s Rule as a Mechanism for Fluorescent Molecular Rotors and Aggregation-Induced Emission. *Nat. Chem.* **2017**, 9, 83.

(16) Ryu, N.; Okazaki, Y.; Pouget, E.; Takafuji, M.; Nagaoka, S.; Ihara, H.; Oda, R. Fluorescence Emission Originated from the H-aggregated Cyanine Dye with Chiral Gemini Surfactant Assemblies Having a Narrow Absorption Band and a Remarkably Large Stokes Shift. *Chem. Commun.* **2017**, 53, 8870–8873.

(17) Kasha, M. Characterization of Electronic Transitions in Complex Molecules. Disc. Faraday Soc. **1950**, 9, 14–19.

(18) Sato, T. Fluorescence via Reverse Intersystem Crossing from Higher Triplet States. J. Comput. Chem. Jpn. **2016**, 14, 189–192.

(19) Sato, T.; Hayashi, R.; Haruta, N.; Pu, Y.-J. Fluorescence via Reverse Intersystem Crossing from Higher Triplet States in a Bisanthracene Derivative. Sci. Rep. **2017**, 7, 4820.

(20) Pu, Y.-J.; Satake, R.; Koyama, Y.; Otomo, T.; Hayashi, R.; Haruta, N.; Katagiri, H.; Otsuki, D.; Kim, D.; Sato, T. Absence of Delayed Fluorescence and Triplet–Triplet Annihilation in Organic Light Emitting Diodes with Spatially Orthogonal Bisanthracenes. J. Mater. Chem. C **2019**, 7, 2541–2547.

(21) Endo, A.; Ogasawara, M.; Takahashi, A.; Yokoyama, D.; Kato, Y.; Adachi, C. Thermally activated delayed fluorescence from Sn⁴⁺–porphyrin complexes and their application to organic light emitting diodes—A novel mechanism for electroluminescence. Adv. Mater. **2009**, 21, 4802–4806.

(22) Adachi, C. Third-Generation Organic Electroluminescence Materials. Jpn. J. Appl. Phys. **2014**, 53, 060101.

(23) Hu, J.-Y.; Pu, Y.-J.; Satoh, F.; Kawata, S.; Katagiri, H.; Sasabe, H.; Kido, J. Bisanthracene-Based Donor–Acceptor-type Light-Emitting Dopants: Highly Efficient Deep-Blue Emission in Organic Light-Emitting Devices. Adv. Funct. Mater. **2014**, 24, 2064–2071.

(24) Nishio, S.; Higashiguchi, K.; Matsuda, K. The Effect of Cyano Substitution on the Fluorescence Behavior of 1,2-Bis(pyridylphenyl)ethene. Asian J. Org. Chem. **2014**, 3, 686–690.

(25) Shizu, K.; Sato, T.; Tanaka, K. Inverse Relationship of Reorganization Energy to The Number of π Electrons from Perspective of Vibronic Coupling Density. J. Comput. Chem. Jpn. **2013**, 12, 215–221.

(26) Sato, T.; Tokunaga, K.; Tanaka, K. Vibronic Coupling in Naphthalene Anion: Vibronic Coupling Density Analysis for Totally Symmetric Vibrational Modes. J. Phys. Chem. A **2008**, 112, 758–767.

(27) Sato, T.; Tokunaga, K.; Iwahara, N.; Shizu, K.; Tanaka, K. Vibronic Coupling Constant and Vibronic Coupling Density. In The Jahn-Teller Effect: Fundamentals and Implications for Physics and Chemistry; Köppel, H., Yarkony, D. R., Barentzen, H., Eds.; Springer-Verlag: Berlin and Hidelberg, 2009; pp 99–129.

(28) Sato, T.; Uejima, M.; Iwahara, N.; Haruta, N.; Shizu, K.; Tanaka, K. Vibronic Coupling Density and Related Concepts. J. Phys.: Conf. Ser. **2013**, 428, 012010.

(29) Fischer, G. Vibronic Coupling: The Interaction between the Electronic and Nuclear Motions; Academic Press: London, 1984.

(30) Azumi, T.; Matsuzaki, K. What Does the Term "Vibronic Coupling" Mean? Photochem. Photobiol. **1977**, 25, 315–326.

(31) Uejima, M.; Sato, T.; Yokoyama, D.; Tanaka, K.; Park, J.-W. Quantum Yield in Blue-Emitting Anthracene Derivatives: Vibronic Coupling Density and Transition Dipole Moment Density. Phys. Chem. Chem. Phys. **2014**, 16, 14244–14256.

(32) Hutchisson, E. Band spectra intensities for symmetrical diatomic molecules. Phys. Rev. **1930**, 36, 410.

(33) Svensson, M.; Humbel, S.; Froese, R. D.; Matsubara, T.; Sieber, S.; Morokuma, K. ONIOM: a multilayered integrated MO+ MM method for geometry optimizations and

single point energy predictions. A test for Diels- Alder reactions and Pt (P (t-Bu) 3) 2+ H2 oxidative addition. J. Phys. Chem. **1996**, 100, 19357–19363.

(34) Chung, L. W.; Sameera, W.; Ramozzi, R.; Page, A. J.; Hatanaka, M.; Petrova, G. P.; Harris, T. V.; Li, X.; Ke, Z.; Liu, F.; Li, H.-B.; Ding, L.; Morokuma, K. The ONIOM Method and its Applications. Chem. Rev. **2015**, 115, 5678–5796.

(35) Tomasi, J.; Mennucci, B.; Cammi, R. Quantum mechanical continuum solvation models. Chem. Rev. **2005**, 105, 2999–3094.

(36) Frisch, M. J.; Trucks, G. W.; Schlegel, H. B.; Scuseria, G. E.; Robb, M. A.; Cheeseman, J. R.; Scalmani, G.; Barone, V.; Mennucci, B.; Petersson, G. A.; Nakatsuji, H.; Caricato, M.; Li, X.; Hratchian, H. P.; Izmaylov, A. F.; Bloino, J.; Zheng, G.; Sonnenberg, J. L.; Hada, M.; Ehara, M.; Toyota, K.; Fukuda, R.; Hasegawa, J.; Ishida, M.; Nakajima, T.; Honda, Y.; Kitao, O.; Nakai, H.; Vreven, T.; Montgomery Jr., J. A.; Peralta, J. E.; Ogliaro, F.; Bearpark, B.; J, H. J.; Brothers, E.; Kudin, K. N.; Staroverov, V. N.; Keith, T.; Kobayashi, R.; Normand, J.; Raghavachari, K.; Rendell, A.; Burant, J. C.; Iyengar, S. S.; Tomasi, J.; Cossi, M.; Rega, N.; Millam, J. M.; Klene, M.; Knox, J. E.; Cross, J. B.; Bakken, V.; Adamo, C.; Jaramillo, J.; Gomperts, R.; Stratmann, R. E.; Yazyev, O.; Austin, A. J.; Cammi, R.; Pomelli, C.; Ochterski, J. W.; Martin, R. L.; Morokuma, K.; Zakrzewski, V. G.; Voth, G. A.; Salvador, P.; Dannenberg, J. J.; Dapprich, S.; Daniels, A. D.; Farkas, O.; Foresman, J. B.; Ortiz, J. V.; Cioslowski, J.; Fox, D. J. Gaussian 09, Revision D. 01, Gaussian, Inc.: Wallingford, CT, 2013.

(37) Frisch, M. J.; Trucks, G. W.; Schlegel, H. B.; Scuseria, G. E.; Robb, M. A.; Cheeseman, J. R.; Scalmani, G.; Barone, V.; Mennucci, B.; Petersson, G. A.; Nakatsuji, H.; Caricato, M.; Li, X.; Hratchian, H. P.; Izmaylov, A. F.; Bloino, J.; Zheng, G.; Sonnenberg, J. L.; Hada, M.; Ehara, M.; Toyota, K.; Fukuda, R.; Hasegawa, J.; Ishida, M.; Nakajima, T.; Honda, Y.; Kitao, O.; Nakai, H.; Vreven, T.; Montgomery Jr., J. A.;

Peralta, J. E.; Ogliaro, F.; Bearpark, B.; J, H. J.; Brothers, E.; Kudin, K. N.; Staroverov, V. N.; Keith, T.; Kobayashi, R.; Normand, J.; Raghavachari, K.; Rendell, A.; Burant, J. C.; Iyengar, S. S.; Tomasi, J.; Cossi, M.; Rega, N.; Millam, J. M.; Klene, M.; Knox, J. E.; Cross, J. B.; Bakken, V.; Adamo, C.; Jaramillo, J.; Gomperts, R.; Stratmann, R. E.; Yazyev, O.; Austin, A. J.; Cammi, R.; Pomelli, C.; Ochterski, J. W.; Martin, R. L.; Morokuma, K.; Zakrzewski, V. G.; Voth, G. A.; Salvador, P.; Dannenberg, J. J.; Dapprich, S.; Daniels, A. D.; Farkas, O.; Foresman, J. B.; Ortiz, J. V.; Cioslowski, J.; Fox, D. J. Gaussian 09, Revision E. 01, Gaussian, Inc.: Wallingford, CT, 2013.

(38) Sato, T.; Iwahara, N.; Haruta, N.; Tanaka, K. C₆₀ bearing ethylene moieties. Chem. Phys. Lett. **2012**, 531, 257–260.

(39) Yeh, H.-C.; Wu, W.-C.; Wen, Y.-S.; Dai, D.-C.; Wang, J.-K.; Chen, C.-T. Derivative of α , β -Dicyanostilbene: Convenient Precursor for the Synthesis of Diphenylmaleimide Compounds, E-Z Isomerization, Crystal Structure, and Solid-State Fluorescence. J. Org. Chem. **2004**, 69, 6455–6462.

(40) Li, Y.; Li, F.; Zhang, H.; Xie, Z.; Xie, W.; Xu, H.; Li, B.; Shen, F.; Ye, L.; Hanif, M.; Ma, D.; Ma, Y. Tight Intermolecular Packing through Supramolecular Interactions in Crystals of Cyano Substituted Oligo(para-phenylene Vinylene): a Key Factor for Aggregation-Induced Emission. Chem. Commun. **2007**, 231–233.

Supporting Information

Origin of Aggregation-Induced Enhanced Emission: A Role of Pseudo-Degenerate Electronic States of Excimers Formed in Aggregation Phases

Wataru Ota,^{a,b} Ken Takahashi,^c Kenji Higashiguchi,^d

Kenji Matsuda,^d and Tohru Sato,^{*a,b,e}

December 24, 2019

^a Fukui Institute for Fundamental Chemistry, Kyoto University, Sakyo-ku, Kyoto 606-8103, Japan;

^b Department of Molecular Engineering, Graduate School of Engineering, Kyoto University, Nishikyo-ku, Kyoto 615-8510, Japan

^c Undergraduate School of Industrial Chemistry, Faculty of Engineering, Kyoto University, Nishikyo-ku, Kyoto 615-8510, Japan

^d Department of Molecular Engineering, Graduate School of Engineering, Kyoto University, Nishikyo-ku, Kyoto 615-8510, Japan

^e Unit of Elements Strategy Initiative for Catalysts & Batteries, Kyoto University, Nishikyo-ku, Kyoto 615-8510, Japan

E-mail: tsato@scl.kyoto-u.ac.jp

Contents

S1 Dimer Models in Solid Phase	3
S2 Irreducible Representations of Excimers	4
S2.1 C_i symmetry	4
S2.2 C_2 symmetry	5
S2.3 C_s symmetry	6
S3 Electron Density Differences of Dimer Model 2 and 3	7
S4 Potential Derivatives of Monomer Model and Dimer Model 1	8
S5 Potential Energy Surface of Monomer Model	9
S6 Decamer Model in Solid Phase	10
S7 Hubbard Model of a Pseudo-Degenerate Electronic System	12

S1 Dimer Models in Solid Phase

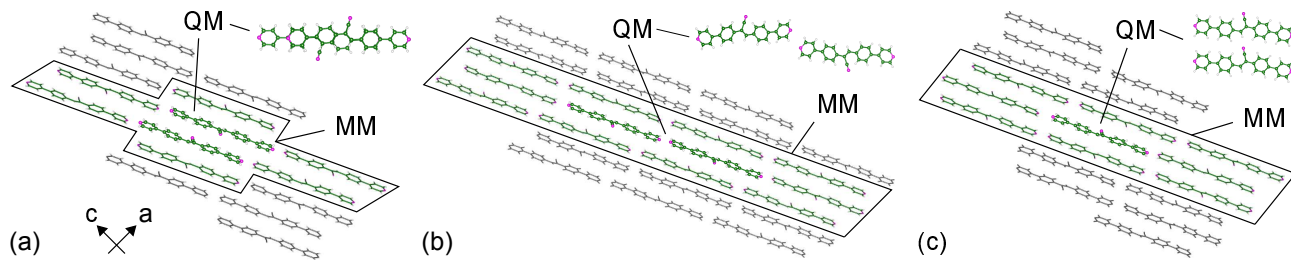


Fig. S1 Dimer Model (a) **1**, (b) **2**, and (c) **3** for the CNBE solid. In Dimer Model **2**, a dimer aligned in a *ca*-plane was selected as the QM region and the surrounding 38 molecules were selected as the MM region. In Dimer Model **3**, a dimer aligned in a *b*-direction was selected as the QM region and the surrounding 29 molecules were selected as the MM region. The QM region was computed at the M06-2X/6-31G(d,p) levels of theory and the MM region was computed using the UFF.

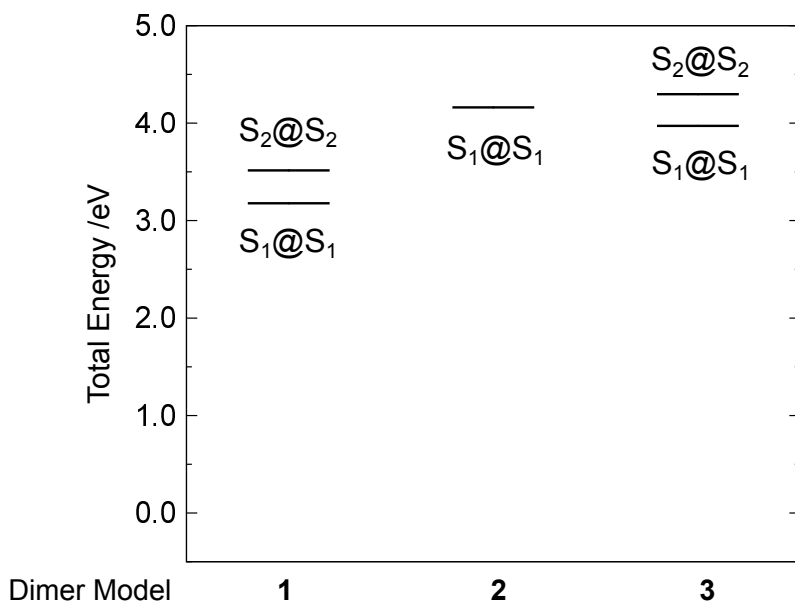


Fig. S2 Total energy of excited states of Dimer Model **1**, **2**, and **3** in the QM region. The energy reference is the total energy of $S_0 @ S_0$ of Dimer Model **1**, -2253.41783105 a.u.

S2 Irreducible Representations of Excimers

S2.1 C_i symmetry

Table S1 tabulates the character table of C_i point group¹. In C_i point group, there are the cases where an atom does not exist on the inversion center and where an atom exists on the inversion center. When an atom does not exist on the inversion center, the reducible representation of vibrational modes is decomposed as

$$\Gamma_{\text{vib}} = \frac{3N-6}{2}A_g + \frac{3N-6}{2}A_u, \quad (1)$$

where N denotes the number of atoms. The half of the vibrational modes belongs to A_g and the other half to A_u . On the other hand, when an atom exists on the inversion center, the number of the vibrational modes is

$$\Gamma_{\text{vib}} = \frac{3N-9}{2}A_g + \frac{3N-3}{2}A_u. \quad (2)$$

The numbers of the vibrational modes belonging to A_g and A_u are different.

Table S1 Character table of C_i point group.

C_i	E	i		$h=2$
A_g	1	1	R_x, R_y, R_z	$x^2, y^2, z^2, xy, yz, zx$
A_u	1	-1		x, y, z

S2.2 C_2 symmetry

Table S2 tabulates the character table of C_2 point group¹. In C_2 point group, there are the cases where no atoms are on a rotational axis and where atoms are on a rotational axis. When atoms are not on a rotational axis, the reducible representation of vibrational modes is decomposed as

$$\Gamma_{\text{vib}} = \frac{3N-4}{2}A + \frac{3N-8}{2}B. \quad (3)$$

The numbers of the vibrational modes belonging to A and B are not the same. When N_a atoms are on a rotational axis, the number of the vibrational modes is

$$\Gamma_{\text{vib}} = \frac{3N-N_a-4}{2}A + \frac{3N+N_a-8}{2}B. \quad (4)$$

The number of the vibrational modes belonging to B increases with N_a .

Table S2 Character table of C_2 point group.

C_2	E	C_2		$h=2$
A	1	1	z, R_z	x^2, y^2, z^2, xy
B	1	-1	x, y, R_x, R_y	yz, zx

S2.3 C_s symmetry

Table S3 tabulates the character table of C_s point group¹. In C_s point group, there are the cases where no atoms are on a mirror plane and where atoms are on a mirror plane. When atoms are not on a mirror plane, the reducible representation of vibrational modes is decomposed as

$$\Gamma_{\text{vib}} = \frac{3N-6}{2}A' + \frac{3N-6}{2}A''. \quad (5)$$

The half of the vibrational modes belongs to A' and the other half to A'' . When N_p atoms are on a mirror plane, the number of the vibrational modes is

$$\Gamma_{\text{vib}} = \frac{3N+N_p-6}{2}A' + \frac{3N-N_p-6}{2}A''. \quad (6)$$

The number of the vibrational modes belonging to A' increases with N_p .

Table S3 Character table of C_s point group.

C_s	E	σ_h	$h=2$	
A'	1	1	x, y, R_z	x^2, y^2, z^2, xy
A''	1	-1	z, R_x, R_y	yz, zx

S3 Electron Density Differences of Dimer Model 2 and 3

Table S4 Excited states of Dimer Model 2 at the S_0 and S_1 optimized structures.

State	Excitation energy		<i>f</i>	Major Configuration (CI Coefficient)
	eV	nm		
@ S_0	S_1 (A)	3.8692	320.44	3.2829 HO-1 \rightarrow LU (0.398), HO \rightarrow LU+1 (0.565)
	S_2 (A)	3.9294	315.53	0.0977 HO-1 \rightarrow LU (0.565), HO \rightarrow LU+1 (-0.399)
@ S_1	S_1 (A)	3.1122	398.39	1.8360 HO \rightarrow LU (0.700)
	S_2 (A)	3.9107	317.04	1.5560 HO-1 \rightarrow LU+1 (0.791)

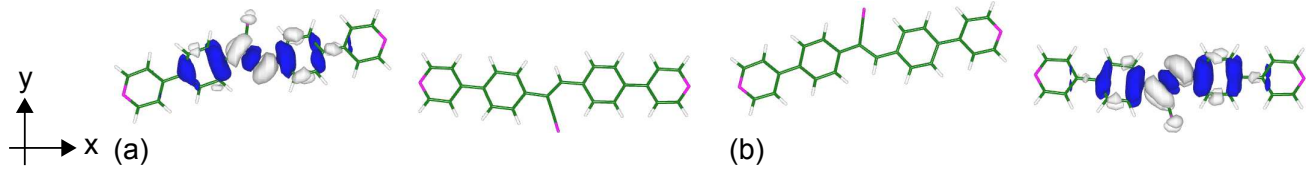


Fig. S3 Electron density differences of (a) S_1 @ S_1 - S_0 @ S_1 and (b) S_2 @ S_1 - S_0 @ S_1 for Dimer Model 2. Isosurface values are 1.0×10^{-3} a.u.

Table S5 Excited states Dimer Model 3 at the S_0 and S_2 optimized structures.

State	Excitation energy		<i>f</i>	Major Configuration (CI Coefficient)
	eV	nm		
@ S_0	S_1 (A)	3.7862	327.46	0.1146 HO-1 \rightarrow LU (0.57769), HO \rightarrow LU+1 (-0.37639)
	S_2 (A)	3.9346	315.12	2.6588 HO-1 \rightarrow LU (0.38099), HO \rightarrow LU+1 (0.57373)
@ S_2	S_1 (A)	3.3696	367.95	0.0005 HO-1 \rightarrow LU (0.49586), HO \rightarrow LU+1 (-0.48388)
	S_2 (A)	3.5310	351.13	2.8119 HO-1 \rightarrow LU (0.48848), HO \rightarrow LU+1 (0.49548)

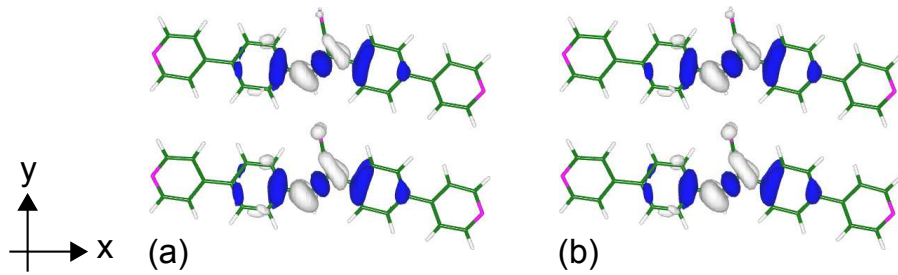


Fig. S4 Electron density differences of (a) S_1 @ S_2 - S_0 @ S_2 and (b) S_2 @ S_2 - S_0 @ S_2 for Dimer Model 3. Isosurface values are 1.0×10^{-3} a.u.

S4 Potential Derivatives of Monomer Model and Dimer Model 1

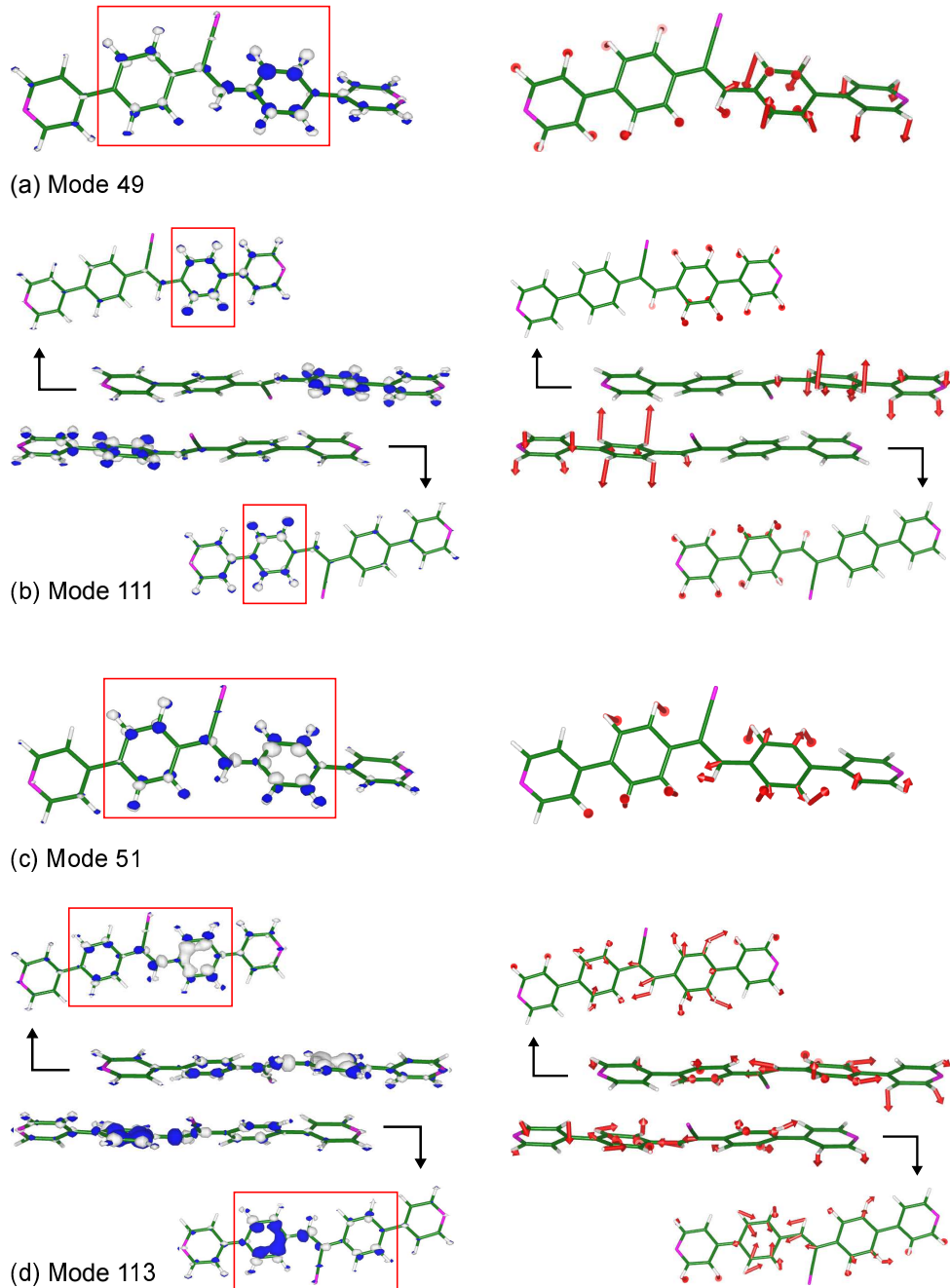


Fig. S5 Potential derivatives of (a) mode 49 for Monomer Model and (b) mode 111 for Dimer Model 1 of which the off-diagonal VCC is reduced by the packing effect. Potential derivatives of (c) mode 51 for Monomer Model and (d) mode 113 for Dimer Model 1 of which the off-diagonal VCC is not reduced by the packing effect. Isosurface value for Monomer Model is 1×10^{-2} a.u. and for Dimer Model 1 is $1/\sqrt{2} \times 10^{-2}$ a.u.

S5 Potential Energy Surface of Monomer Model

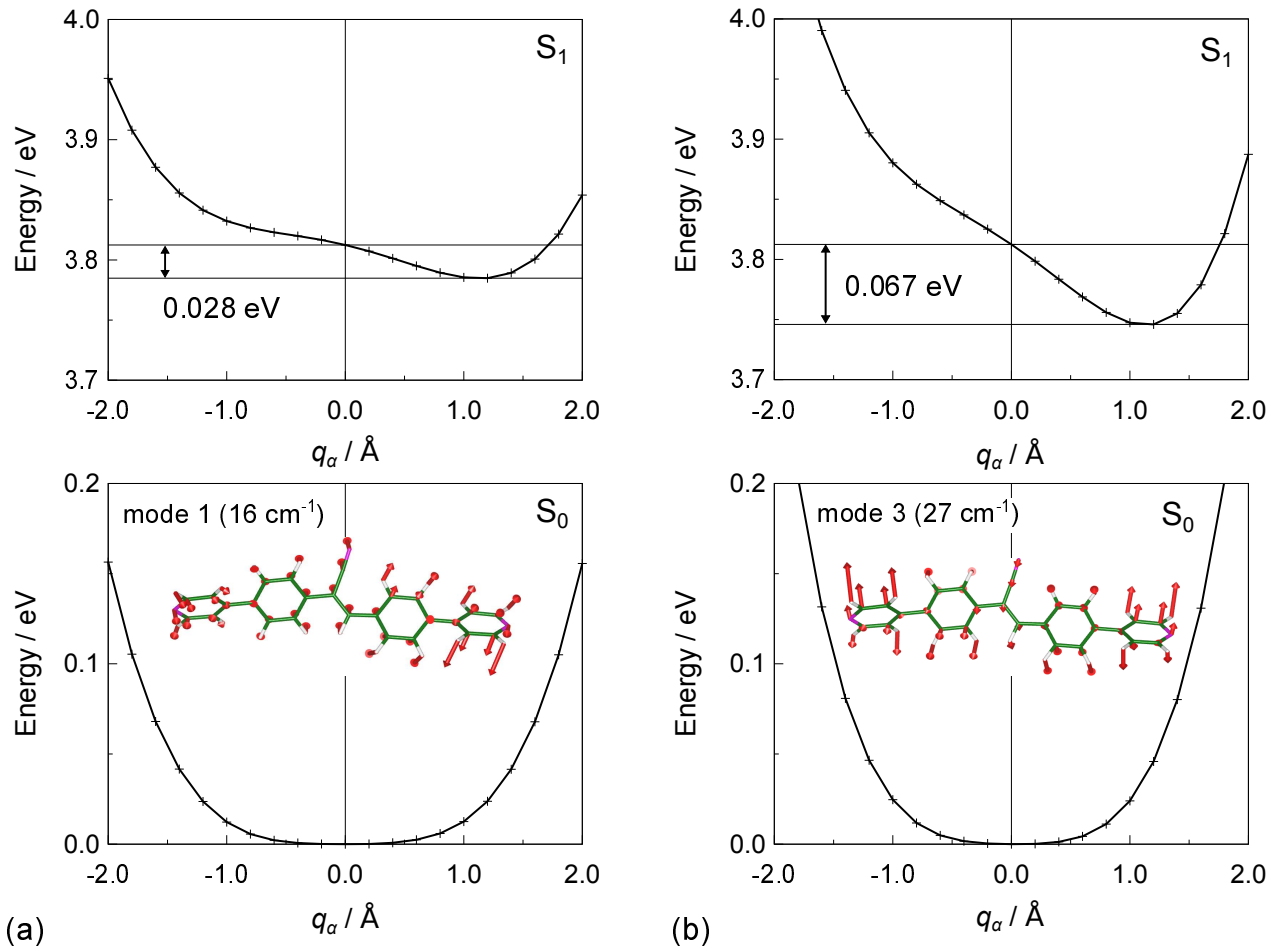


Fig. S6 Potential energy surfaces of S_0 and S_1 of Monomer Model along with (a) mode 1 and (b) mode 3. q_α denotes the Cartesian displacement from the S_0 optimized structure. The potential energy surfaces along with these modes were not approximated to harmonic potentials. The reorganization energies of modes 1 and 3 including the anharmonicity effect were calculated to be 0.028 and 0.067 eV, respectively.

S6 Decamer Model in Solid Phase

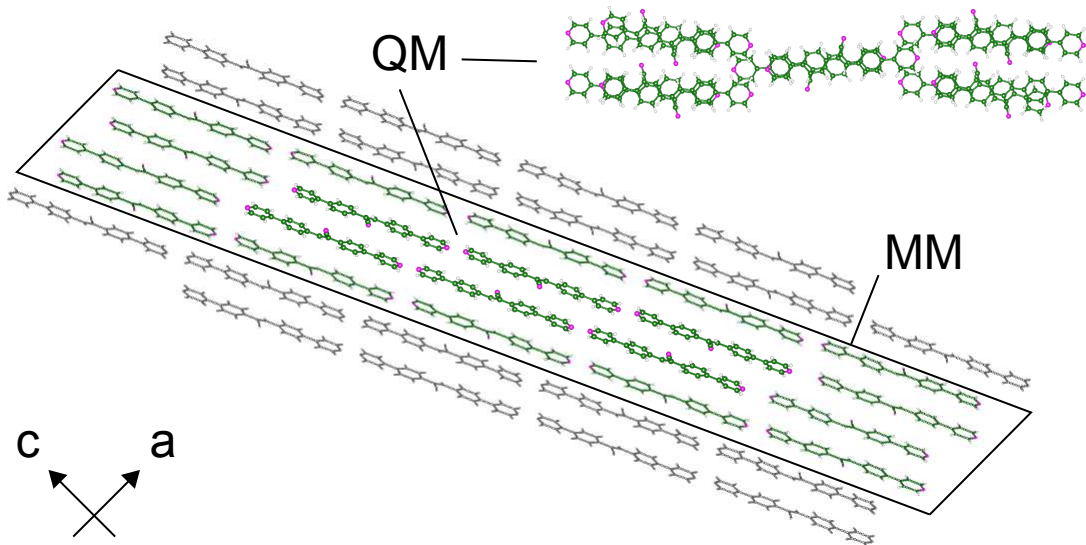


Fig. S7 Decamer Model for the CNBE solid. Centered decamer is selected as the QM region (M06-2X/3-21G) and the surrounding 60 molecules are selected as the MM region (UFF).

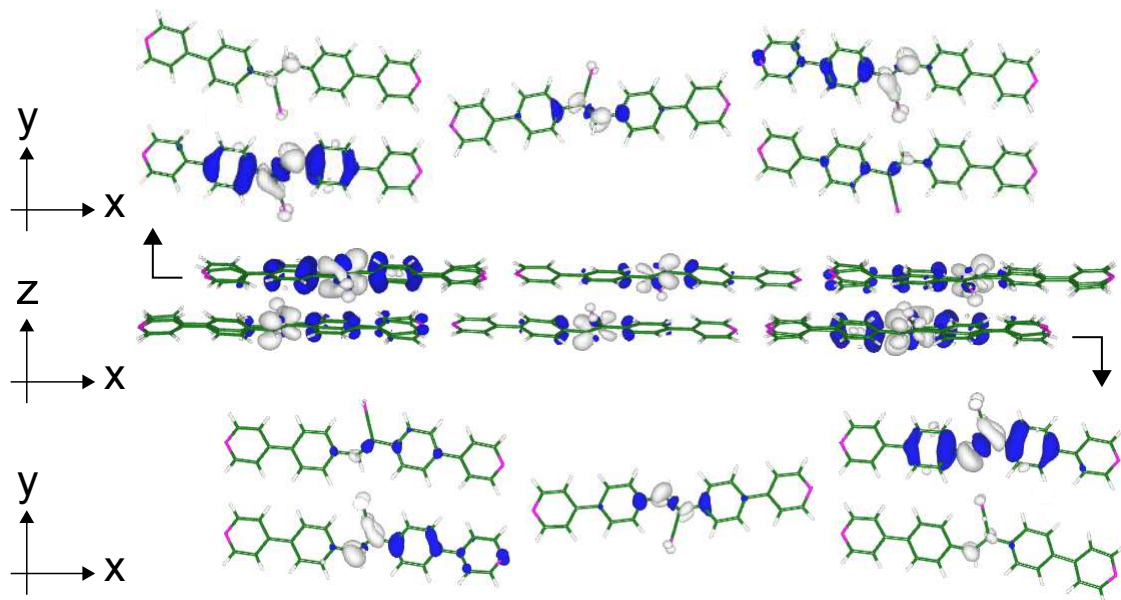


Fig. S8 Electron density difference of $S_8@S_0 - S_0@S_0$ for Decamer Model. Isosurface value is 3.0×10^{-4} a.u.

Table S6 Excited states of Decamer Model at the S₀ optimized structure.

State	Excitation energy		<i>f</i>	Major Configuration (CI Coefficient)
	eV	nm		
S ₁ (A _u)	3.7447	331.09	0.0052	HO-4 → LU (0.2715), HO-4 → LU+5 (-0.2389) HO-3 → LU+1 (-0.2715), HO-3 → LU+4 (-0.2389)
S ₂ (A _g)	3.7447	331.09	0.0000	HO-4 → LU+1 (0.2717), HO-4 → LU+4 (0.2392) HO-3 → LU (-0.2717), HO-3 → LU+5 (0.2392)
S ₃ (A _g)	3.7775	328.21	0.0000	HO-4 → LU+1 (0.2197), HO-3 → LU (-0.2199) HO-2 → LU+3 (0.2583), HO-1 → LU+2 (0.2583)
S ₄ (A _u)	3.7775	328.21	0.0618	HO-4 → LU (-0.2204), HO-3 → LU+1 (0.2204) HO-2 → LU+2 (0.2580), HO-1 → LU+3 (0.2580)
S ₅ (A _u)	3.8860	319.06	0.7377	HO-4 → LU+2 (-0.2070), HO-4 → LU+5 (0.2771) HO-3 → LU+3 (-0.2070), HO-3 → LU+4 (0.2771) HO-2 → LU+6 (-0.2052), HO-1 → LU+7 (0.2052)
S ₆ (A _g)	3.8871	318.96	0.0000	HO-4 → LU+3 (-0.2030), HO-4 → LU+4 (0.2690) HO-3 → LU+2 (-0.2030), HO-3 → LU+5 (0.2690) HO-2 → LU+7 (0.2208), HO-1 → LU+6 (-0.2208)
S ₇ (A _g)	3.9259	315.81	0.0000	HO-5 → LU+9 (-0.2354), HO → LU+8 (0.6484)
S ₈ (A _u)	3.9942	310.41	9.0385	HO-2 → LU+6 (-0.3474), HO-1 → LU+7 (0.3474) HO → LU+9 (-0.2498)
S ₉ (A _g)	4.0290	307.73	0.0000	HO-2 → LU+7 (-0.3649), HO-1 → LU+6 (0.3649)
S ₁₀ (A _u)	4.1224	300.76	1.1521	HO → LU+9 (-0.5282)

S7 Hubbard Model of a Pseudo-Degenerate Electronic System

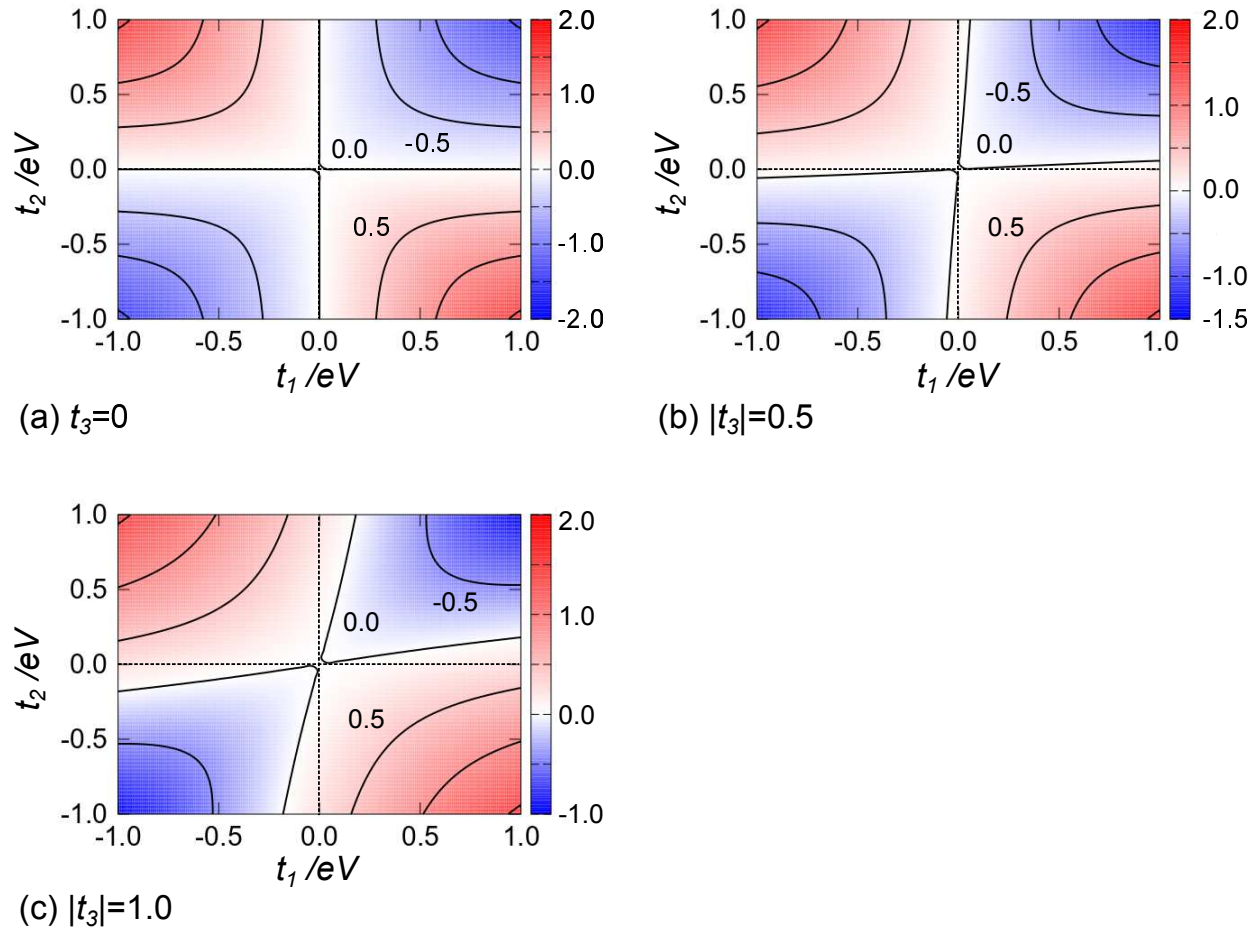


Fig. S9 Energy difference between first and second excited states, $E_1^s - E_1^a$, calculated by numerically diagonalizing the Hubbard Hamiltonian. ε , U_1 , and U_2 were set to 3.0, 1.0, and 1.0, respectively.

In this section, we describe the electron density differences and overlap densities in the pseudo-degenerate electronic system using the Hubbard model. The electron density in the ground state is defined by ρ_0 . The orbital overlap densities are defined by

$$p_1 = |\phi_{\text{HO}}(X_1)|^2, \quad p_2 = |\phi_{\text{HO}}(X_2)|^2, \quad q_1 = |\phi_{\text{LU}}(X_1)|^2, \quad q_2 = |\phi_{\text{LU}}(X_2)|^2, \quad (7)$$

$$r_1 = \phi_{\text{HO}}(X_1)\phi_{\text{LU}}(X_1), \quad r_2 = \phi_{\text{HO}}(X_2)\phi_{\text{LU}}(X_2), \quad (8)$$

$$s_1 = \phi_{\text{HO}}(X_1)\phi_{\text{HO}}(X_2), \quad s_2 = \phi_{\text{LU}}(X_1)\phi_{\text{LU}}(X_2), \quad s_3 = \phi_{\text{HO}}(X_1)\phi_{\text{LU}}(X_2) = \phi_{\text{LU}}(X_1)\phi_{\text{HO}}(X_2), \quad (9)$$

where $\phi_{\text{HO/LU}}(X_1/X_2)$ represent the HOMO/LUMO of X_1/X_2 . The overlaps between X_1 and X_2 separated from each other, namely s_1 , s_2 and s_3 , are supposed to be 0. Table S7 and S8 tabulate the electron density differences and overlap densities in the pseudo-degenerate electronic system.

Table S7 Electron density differences in the pseudo-degenerate system. $\alpha = \frac{1}{2}((\rho_0 - p_1 + q_1) + (\rho_0 - p_2 + q_2))$. For Dimer Model **1** of the CNBE solid, S_1 corresponds to $|\Psi_1^s\rangle$, and S_2 $|\Psi_1^a\rangle$. Therefore, the electron density difference between S_1 and S_2 is given by 0.

	Ψ_0	Ψ_1^s	Ψ_2^s	Ψ_1^a	Ψ_2^a
Ψ_0	0	$\rho_0 - \alpha$	$\rho_0 - \alpha$	$\rho_0 - \alpha$	$\rho_0 - \alpha$
Ψ_1^s		0	0	0	0
Ψ_2^s			0	0	0
Ψ_1^a				0	0
Ψ_2^a					0

Table S8 Overlap densities in the pseudo-degenerate system. $\alpha = \frac{1}{2}((\rho_0 - p_1 + q_1) + (\rho_0 - p_2 + q_2))$, $\beta_1 = \frac{1}{2}(q_1 - p_1 - q_2 + p_2) \approx 0$, $\beta_2 = \frac{1}{2}(q_2 - p_1 - q_1 + p_2)$, $\gamma_1 = \frac{1}{\sqrt{2}}(r_1 + r_2)$, $\gamma_2 = \frac{1}{\sqrt{2}}(r_1 - r_2)$. For Dimer Model **1** of the CNBE solid, S_1 corresponds to $|\Psi_1^s\rangle$, and S_2 $|\Psi_1^a\rangle$. Therefore, the overlap density between S_1 and S_2 is given by $\beta_1 \approx 0$.

	Ψ_0	Ψ_1^s	Ψ_2^s	Ψ_1^a	Ψ_2^a
Ψ_0	ρ_0	γ_1	$\frac{t_1+t_2}{U_2}\gamma_1 - \frac{t_3}{\varepsilon - U_1 + 2U_2}\alpha$	γ_2	$\frac{t_2-t_1}{U_2}\gamma_2 - \frac{t_3}{\varepsilon - U_1 + 2U_2}\beta_2$
Ψ_1^s		α	0	$\beta_1 (\approx 0)$	$\frac{t_2-t_1}{U_2}\beta_1 - \frac{t_1+t_2}{U_2}\beta_2$
Ψ_2^s			α	$\frac{t_1+t_2}{U_2}\beta_1 - \frac{t_2-t_1}{U_2}\beta_2$	β_2
Ψ_1^a				α	0
Ψ_2^a					α

References

- 1 Atkins, P.; Overton, T.; Rourke, J.; Weller, J.; Armstrong, F. Shriver and Atkins' Inorganic Chemistry, 5th ed.; Oxford University Press, USA, 2010.